AAS 17-744

THE NEAR-EARTH ASTEROID CHARACTERIZATION AND OBSERVATION (NEACO) MISSION

Chandrakanth Venigalla,[*] Nicola Baresi,[*] Jonathan Aziz,[*] Benjamin Bercovici,[*] Gabriel Borderes Motta,[†] Daniel Brack,[*] Josué Cardoso dos Santos,[†] Andrew Dahir,[*] Alex B. Davis,[*] Stijn De Smet,[*] JoAnna Fulton,[*] Nathan Parrish,[*] Marielle Pellegrino,[*] Stefaan Van wal[*]

The Near-Earth Asteroid Characterization and Observation (NEACO) mission proposes to explore the fast-rotating asteroid (469219) 2016 HO_3 with a SmallSat spacecraft and perform an early scientific investigation to enable future, more in-depth missions. The NEACO spacecraft is equipped with a low-thrust, solar electric propulsion system to reach its target within two years, making use of an Earth gravity assist. Its instrument suite consists of two optical cameras, a spectrometer, an altimeter, and an explosive impactor assembly. Upon arrival at HO_3, NEACO uses pulsed plasma thrusters to hover, first at a high altitude of 50 km to perform lit surface mapping and shape modeling, and later at a lower altitude of 10 km to refine these models and perform surface spectroscopy. Following the hovering phases, the spacecraft performs several flybys with decreasing periapses in order to estimate the asteroid's mass. Finally, NEACO uses an additional flyby to release an explosive impactor that craters the asteroid surface. After spending a few weeks at a safe hovering distance, the spacecraft returns and images the crater and freshly exposed sub-surface material. This provides information on the strength of the asteroid surface. The science operations are completed within eight months, with the total mission lasting less than three years. The objectives met by the NEACO mission satisfy all science goals for the student competition of the 2017 AAS Astrodynamics Specialist Conference.

INTRODUCTION

The Near-Earth Asteroid Characterization and Observation (NEACO) mission aims to meet the scientific goals outlined in the student competition for the 2017 American Astronautical Society Astrodynamics Specialist Conference. The overall competition goal is to send one or more 140 kg spacecraft to investigate asteroid (469219) 2016 HO_3. The competition guidelines dictate the following assumptions:

- The orbit is defined by JPL Horizons
- The asteroid has dimensions of 100 m x 50 m x 40 m
- The asteroid has a density of 2 g/cm^3
- The spin period is 27 minutes
- The asteroid is S- or Q-type

The following science goals are defined in the competition guidelines (not all must be met):

1. Measure mass to an accuracy of 10%

---

[*] Ph.D. Student, Smead Department of Aerospace Engineering Sciences, University of Colorado, Boulder CO 80309.

[†] Ph.D. Student, Department of Physics,São Paulo State University (UNESP), Guaratinguetá-SP 12516-410, Brazil

2. Measure volume to an accuracy of 10% across a decameter resolution
3. Develop global shape model to 5 m accuracy
4. Map lit surface at 1 m^2 resolution
5. Map at least one 10 m^2 regions at 1 cm^2 resolution
6. Measure spectral properties of surface at a few decameter resolution
7. Characterize the strength of the asteroid surface at one site

To accomplish these goals, the NEACO mission will travel to and characterize HO_3 using a single SmallSat equipped with two optical cameras, a spectrometer, an altimeter, and an explosive impactor. The spacecraft also uses solar electric propulsion, pulsed plasma thrusters, and includes deployable solar panels. The team has prioritized the selection of high TRL and flight proven commercial off the shelf (COTS) technologies that enable quick and cheap spacecraft designs. The selection of the mission concept, spacecraft components and payload is summarized in the following paper, which illustrates the design process of NEACO.

To start off, the team prioritized science goals in order to produce engineering and mission requirements. These constraints produced preliminary mission profiles that were continuously updated based on the instrument selection and better understanding of the dynamical environments near HO_3. The final mission is described in the “Mission Concept” and “Spacecraft Design” sections which describe mission operations and spacecraft hardware respectively. After discussing the final mission, further details on the design methods and challenges for the mission are explored in more detail in the “Design Process” section. Major challenges in the design of the NEACO mission include designing a trajectory to HO_3 and selecting instruments to accomplish all science goals with limited mass, power, and volume. Exploring the dynamical environment around such a small mass to find trajectories that are safe and usable in science investigations is also a major challenge. Lastly, determining and achieving surface strength characterization goals for a body with such a high rotation rate is nontrivial.

SCIENCE GOALS

Science Priorities

The NEACO mission’s high-level goal is to conduct an investigation of asteroid 2016 HO_3 in order to obtain the body’s defining characteristics, as a precursor to more advanced future missions. To achieve this, a set of science goals is identified that ensures a comprehensive survey of the asteroid is performed. Fundamental questions regarding the asteroid size, shape, composition, and surface environment are addressed by these goals, as listed in Table 1. Each goal corresponds to a goal in the contest guidelines, and has an associated priority assigned by the team.

Threshold mission goals define the minimum set of achievements necessary for mission success. They relate to the measurement of elementary asteroid properties whose values must be known within reasonable accuracy in order to allow for the design and planning of more in-depth future missions to asteroid HO_3. More specifically, knowledge of the asteroid mass, volume, and shape is required for accurate spacecraft orbit design, in particular when performing proximity operations. Maps of the asteroid surface significantly increase the feasibility of autonomous spacecraft operations, for example by enabling on-board localization techniques. At a higher level, the asteroid’s low mass and fast rotation rate result in a type of dynamical environment that has never been visited before. Given the asteroid’s proximity to Earth, an exploration of its elementary characteristics may provide invaluable insight into impact threat mitigation and possible resource extraction methods.

The *baseline* mission goals identify deliverables that further enhance the asteroid investigation. The high-resolution mapping of a select surface region will provide details on HO_3's small features, which provide constraints on future missions that plan to operate on the asteroid's surface. Additionally, investigation of the body's spectral properties provides details on its composition that significantly complement a simple density estimate provided by the threshold-level goals.

Finally, the surface strength characterization is designated as an *extended* mission goal, due to its high operational risk. Nevertheless, the strength measurement defines important constraints for the aforementioned mitigation and resource extraction techniques. Spectroscopy of the sub-surface, which may be exposed by strength measuring techniques, would further complement the baseline-level investigation of the asteroid composition.

Table 1. Priority ranking of science goals for the NEACO mission (numbers correspond to competition goals).

Science Goal Deliverable	Mission Priority
1. Mass estimate 2. Volume estimate 3. Global shape model 4. Lit surface map	High/Threshold
5. High-resolution map of 1 region 6. Spectral properties	Mid/Baseline
7. Surface strength	Low/Extended

Science Traceability Matrix

A science traceability matrix (STM) is used to ensure NEACO's instrument suite and mission plan will be able to meet or exceed the science goals presented in Table 1 to the desired resolutions of the competition. The STM is provided in Figure 1, where each row provides a brief but comprehensive overview of which instruments will be used to address the science and measurements, and what the corresponding functional objectives on the instruments are. The STM also includes the resulting data products of the mission design, as a final verification that all mission requirements are met. The competition guidelines quantify the measurement requirements of the mass, volume, shape, and surface mapping objectives. It does not provide a quantified requirement for the surface strength and spectral property objectives. These are therefore defined to best meet the overall objective, where the details of these measurement requirements are determined through extensive literature review as detailed in the respective sections of this paper. The STM illustrates how the science goals of the NEACO mission determined the selected instrument suite. To meet all of the threshold, baseline, and extended mission goals, NEACO is equipped with an altimeter, an optical camera, a spectrometer, and an impactor assembly.

MISSION CONCEPT

Launch, Earth Gravity Assist, and Arrival

The NEACO trajectory includes a low thrust transfer from low Earth orbit to a heliocentric orbit and an Earth gravity assist, with arrival at the Sun-HO_3 L_1 point after two years. A dry mass of 121.1 kg is delivered to HO_3 with a spacecraft wet mass of 140 kg. The trajectory is visualized in Figure 2 using the General Mission Analysis Tool (GMAT).[1] The trajectory starts with a departure

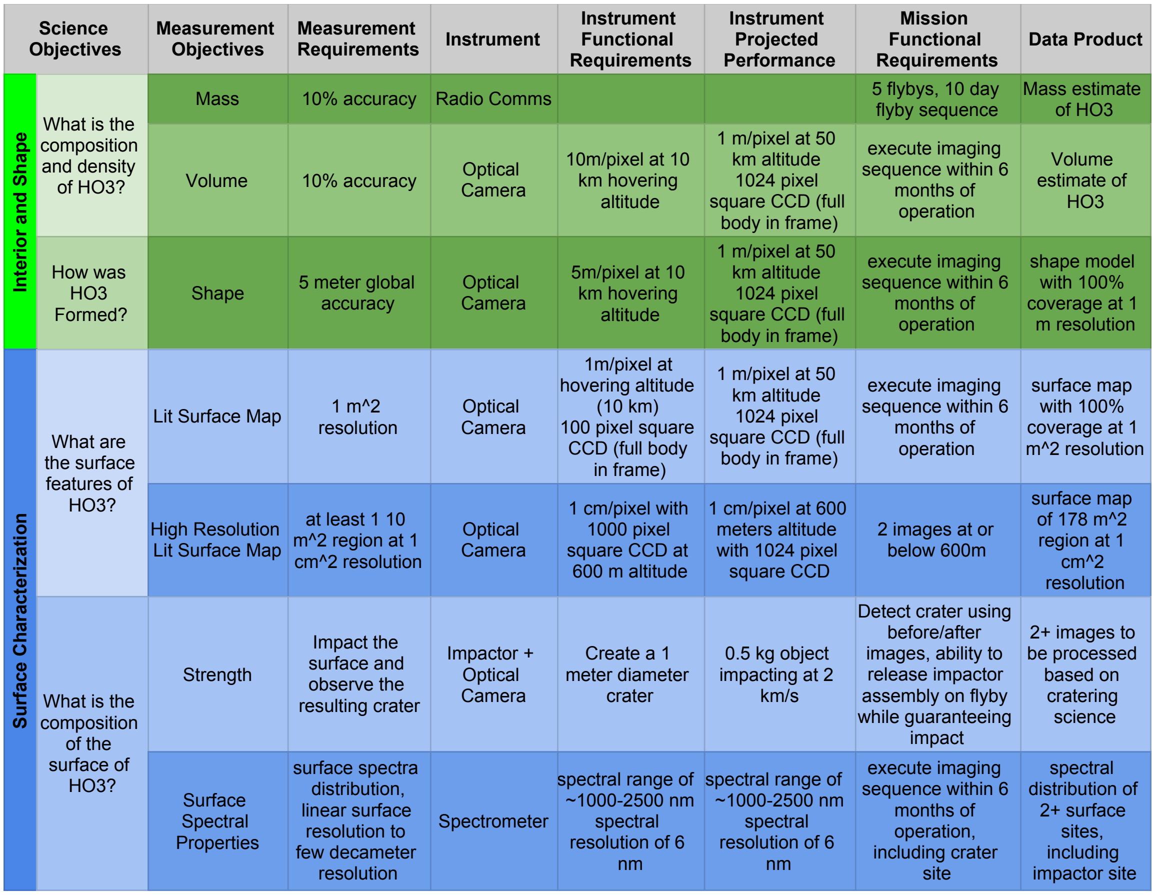

	Science Objectives	Measurement Objectives	Measurement Requirements	Instrument	Instrument Functional Requirements	Instrument Projected Performance	Mission Functional Requirements	Data Product
Interior and Shape	What is the composition and density of HO3?	Mass	10% accuracy	Radio Comms			5 flybys, 10 day flyby sequence	Mass estimate of HO3
		Volume	10% accuracy	Optical Camera	10m/pixel at 10 km hovering altitude	1 m/pixel at 50 km altitude 1024 pixel square CCD (full body in frame)	execute imaging sequence within 6 months of operation	Volume estimate of HO3
	How was HO3 Formed?	Shape	5 meter global accuracy	Optical Camera	5m/pixel at 10 km hovering altitude	1 m/pixel at 50 km altitude 1024 pixel square CCD (full body in frame)	execute imaging sequence within 6 months of operation	shape model with 100% coverage at 1 m resolution
Surface Characterization	What are the surface features of HO3?	Lit Surface Map	1 m^2 resolution	Optical Camera	1m/pixel at hovering altitude (10 km) 100 pixel square CCD (full body in frame)	1 m/pixel at 50 km altitude 1024 pixel square CCD (full body in frame)	execute imaging sequence within 6 months of operation	surface map with 100% coverage at 1 m^2 resolution
		High Resolution Lit Surface Map	at least 1 10 m^2 region at 1 cm^2 resolution	Optical Camera	1 cm/pixel with 1000 pixel square CCD at 600 m altitude	1 cm/pixel at 600 meters altitude with 1024 pixel square CCD	2 images at or below 600m	surface map of 178 m^2 region at 1 cm^2 resolution
	What is the composition of the surface of HO3?	Strength	Impact the surface and observe the resulting crater	Impactor + Optical Camera	Create a 1 meter diameter crater	0.5 kg object impacting at 2 km/s	Detect crater using before/after images, ability to release impactor assembly on flyby while guaranteeing impact	2+ images to be processed based on cratering science
		Surface Spectral Properties	surface spectra distribution, linear surface resolution to few decameter resolution	Spectrometer	spectral range of ~1000-2500 nm spectral resolution of 6 nm	spectral range of ~1000-2500 nm spectral resolution of 6 nm	execute imaging sequence within 6 months of operation, including crater site	spectral distribution of 2+ surface sites, including impactor site

Figure 1. Science traceability matrix of the NEACO mission.

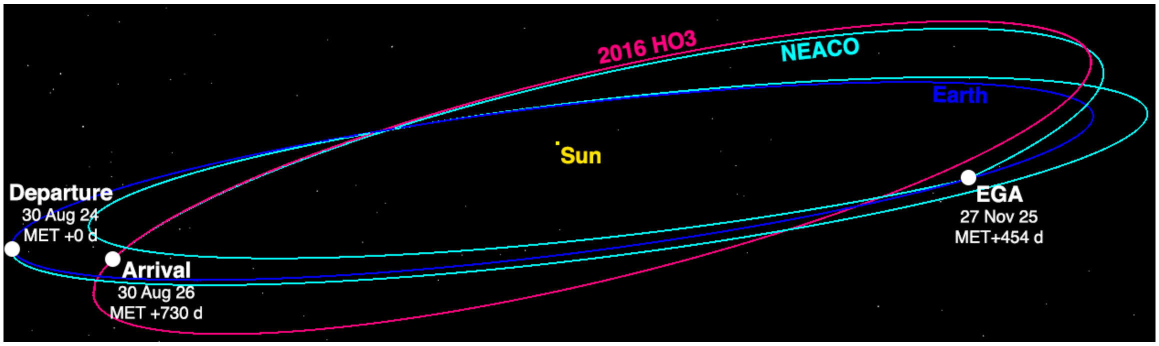

Figure 2. Heliocentric orbit of the NEACO spacecraft.

from a circular LEO orbit with $a = 185$ km and $i = 28.5°$, on August 30, 2024 at 15:05:07 UTC. Following a departure burn from the launch vehicle upper stage, the eccentricity is boosted to $e = 0.9999$. On this coast trajectory, it takes approximately 15.5 days for the spacecraft to reach Earth's sphere of influence, during which the solar electric propulsion (SEP) and subsystems are tested. Thrusting with a 300 W, 8 cm XiPS SEP engine begins on September 15, 2024. A brief 20-day coast arc occurs in July 2025, after which thrusting continues until October 12, 2025; approximately 45 days before the Earth gravity assist (EGA). Final navigation solutions are obtained during the pre-gravity-assist coast, in order to perform the proper B-plane targeting. The EGA occurs at and altitude of 9,935 km with $C_3 = 14.9$ km^2/s^2. This gravity assist increases NEACO's heliocentric inclination from $i = 0.02°$ to $i = 7.07°$. Thrusting resumes 15 days after the EGA and continues until arrival at the Sun-HO$_3$ L_1 point, at approximately 750 km from the asteroid, on August 30, 2026. The final approach is performed on the lit side of the asteroid, to allow for optical target acquisition. This arrival phase will also be used for final instrument checkouts and system checks prior to entering the science phases.

High-Altitude Hovering - 50 km

The first science operations are performed during a hovering phase in which the pulsed plasma thrusters maintain a distance of approximately 50 km to the asteroid. In this phase, the narrow angle camera (NAC) maps the lit surface at the required 1-meter resolution (Goal 4). The same optical images are used to generate the asteroid shape model at a resolution higher than the 5 m accuracy goal (Goals 2 and 3). The asteroid's pole orientation will determine the visible and lit fraction of the asteroid surface, and will be extracted by applying landmark tracking to the NAC images using stereophotoclinometry. Landmark navigation was first demonstrated during the NEAR-Shoemaker mission at asteroid 433 Eros.[2] It was used in combination with stereophotoclinometry during the ESA Rosetta mission about comet Churyumov-Gerasimenko,[3] and will be used by NASA's Osiris-Rex as well.[4] Once the pole orientation has been determined, the scheduling of the remaining imaging sequences can be modified to address the scientific goals. The duration of the high-altitude hovering phase is variable, and will be adjusted following examination of the asteroid's rotation pole and lighting conditions. The absolute maximum duration of this phase is 6 months, which occurs in the case where HO$_3$'s rotation pole is oriented such that one pole will not be illuminated until the asteroid moves to the opposite side of its heliocentric orbit. This is required because a full surface map is ideal for an accurate global shape model. However, in the event that such a pole orientation is found, the bulk of the surface images would be taken from the 50 km altitude, while any remaining images could be taken in the 10 km hovering phase. Note that while this altitude is at the range limit of the altimeter, the altimeter is not critical for navigation here because we can perform optical navigation with the cameras and will be getting tracking data from the ground. Depending on further stability analysis of hovering trajectories, the nominal hovering altitude could also be reduced by several kilometers in order to ensure that the altitude does not drift above 50 km. This change would not require a significant increase in total ΔV required to maintain the hovering trajectory.

Low-Altitude Hovering - 10 km

After completion of the high-altitude hovering phase, the spacecraft descends to a lower altitude of 10 km. The resolution requirements of the surface spectroscopy are met by capturing spectral data at this altitude (Goal 6). The increased resolution of the NAC at this altitude also allows the shape model and surface map to be refined if necessary. At this altitude, both cameras are still able to view the entire asteroid, at a resolution of 15 cm/px for the NAC and 1 m/px for the AMICA camera (backup camera). While this phase provides higher resolution imagery than the previous phase, and could conceivably replace most of the the high-altitude hovering, the increased resolution comes at a cost of larger data files when similar compression is applied. Because of mission bandwidth

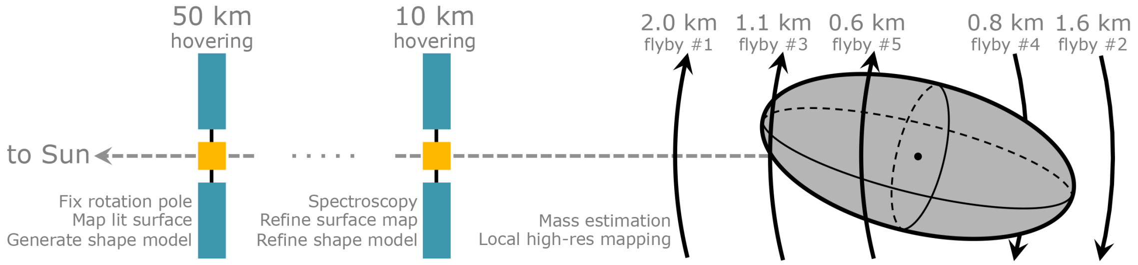

Figure 3. Illustration of the mission concept.

limitations in communicating images back to Earth, this phase is not used for the bulk of surface imaging.

Mass Estimation Flybys

The spacecraft will perform a series of five low-altitude, hyperbolic flybys to estimate the asteroid's mass. The flyby trajectories, as described in Table 8, decrease in incoming hyperbolic velocity from 0.5 to 0.1 m/s and in periapse radius from 2.0 to 0.6 km. The approaches are targeted to the B-plane formed by the Sun-HO_3 and HO_3 orbital angular momentum vectors. The flyby sequences begin and end at a distance of 20 km from the asteroid, ranging in duration from 40 to 10 hours. Including turnaround times of approximately 24 hours, the entire flyby phase lasts for roughly 10 days.

During each flyby, NEACO's laser altimeter provides a distance measurement to confirm the planned flyby geometry. The on-board cameras are also used on each flyby to observe HO_3's surface. The closest flyby allows the NAC to capture images with 1 cm resolution requirement, satisfying the high-resolution imaging goal (Goal 5). Using this flyby series, the 10% accuracy mass estimation goal is satisfied (Goal 1). Following completion of the flybys, the spacecraft returns to the 50 km hovering position while planning for the cratering operation is performed.

Cratering Operation

As the cratering and subsequent imaging operations are some of the highest-risk mission phases, they are the last to be performed before the end of the nominal mission. It is assumed that the surface map produced by prior operations is of sufficiently high resolution to be able to select a target cratering site. Once the site has been selected, the spacecraft is placed on a flyby trajectory with a low periapse. The impactor assembly is ejected opposite the spacecraft orbital velocity, such that its respective trajectory intersects the asteroid surface. Due to the resulting differences in velocity between the spacecraft and impactor assembly, the spacecraft will be above the opposite face of the asteroid when the explosive is detonated using a timer. The asteroid thus effectively shields the spacecraft from high-velocity impact ejecta, as illustrated in Figure 4. This approach is robust, as the spacecraft does not need to perform any post-release maneuvers.

Following detonation, the spacecraft will continue to recede from the asteroid and return to the 50 km hovering position. It will remain there for some amount of time on the order of a few weeks, to wait for small ejecta to be removed from the asteroid's neighborhood by solar radiation pressure. The Hayabusa-2 spacecraft will nominally spend "*more than two weeks*" in such a hold position fol-

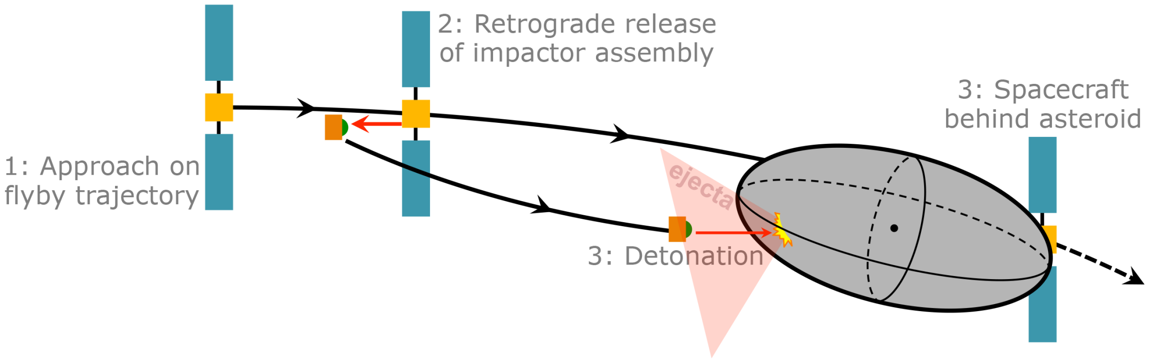

Figure 4. Illustration of the impactor operation.

lowing the detonation of its SCI at asteroid Ryugu.[5] Given that HO_3 is much smaller than Ryugu, such that the relative magnitude of solar radiation pressure is much larger than the asteroid's gravity, this wait time is used as a conservative upper bound. Observations following the cratering experiment on Hayabusa-2 will likely clarify the necessary wait time. Further analysis, following for example Scheeres, Durda, and Geissler[6] may provide context to the expected Hayabusa-2 observations as well.

If the crater produced by NEACO's impactor is sufficiently large, the crater may be visible in one or two pixels from this altitude, where the NAC resolution is roughly 70 cm/px. The spacecraft then descends to the 10 km hovering position, where the surface resolution is 15 cm/px, in order to better resolve the crater. Finally, it performs a flyby at 380 m altitude over the crater, during which both imaging and spectroscopy are performed. At this altitude, a 1 m crater fills the entire field-of-view of the spectrometer. This allows for high-resolution measurements of the freshly exposed subsurface material. Images of the crater can be used to determine its depth and size, which provides information on the compressive strength of the asteroid surface (Goal 7).

SPACECRAFT DESIGN

Instruments

Optical Imaging Suite The optical imaging suite includes the high-resolution NAC and a backup medium-resolution camera (AMICA) for redundancy. Figure 5 plots the altitude at which the different cameras can satisfy the various resolution requirements. The proposed medium-resolution camera is based on the Asteroid Multi-Band Imaging Camera (AMICA) instrument flown on the Hayabusa-1 mission,[7] and the AMICA specifications, included in Table 2, are applied for all imaging related analysis.

In the event of NAC failure, all science goals will still be achievable. Lit surface mapping must then be performed with the AMICA at the low-altitude hovering position in order to achieve the proper resolution. While the AMICA can image the asteroid at a 5 m/px resolution at the high-altitude hovering position for shape model reconstruction, redundant images at a higher resolution would be required at the lower altitude. A close terminator orbit would also be required in order to satisfy the 1 cm/px high-resolution mapping requirement.

The proposed NAC has a narrow overall field of view and a narrow instantaneous field of view

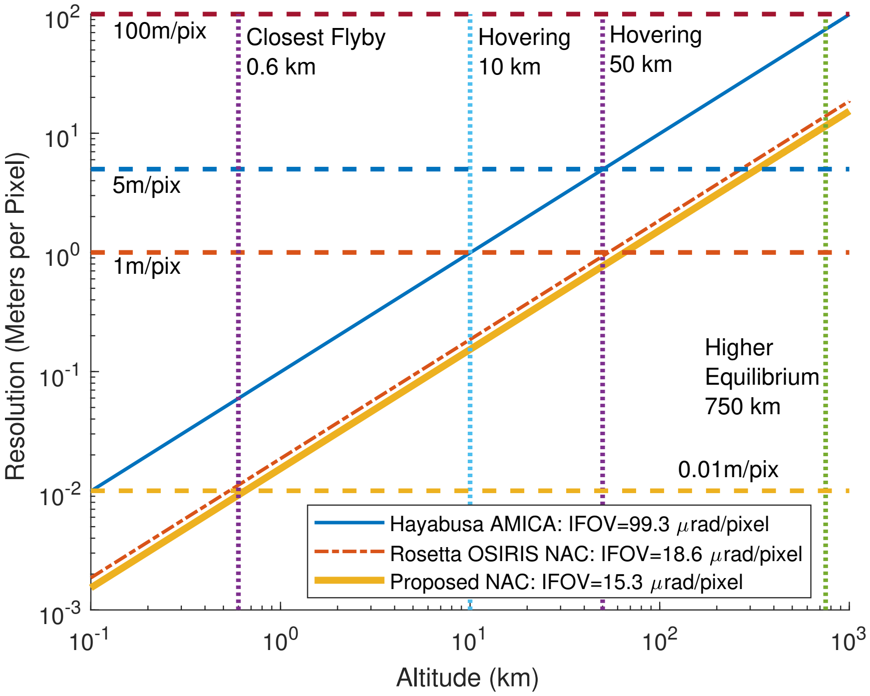

Figure 5. Optical camera resolution at various altitudes.

(IFOV) that enables high-resolution imaging at higher and safer altitudes than the AMICA. The Rosetta OSIRIS NAC is used as an upper bound reference for mass and volume estimation for the proposed NAC. The Rosetta NAC has strict requirements on performance such as stray light rejection for gas and dust imaging[8] that require an optical path with larger footprint than is necessary for NEACO. Thus, the proposed NAC, with a similar IFOV, allows for a similar design with reduced volume and mass requirements. Note that in Table 2, a smaller CCD pixel size can be selected for the proposed NAC to allow for a smaller focal length to meet the required IFOV. Alternative options that may meet the mission requirements include a CubeSat form factor Ritchey-Chrétien telescope[9] or a space-qualified version of a ground telescope with the desired focal length.[10]

Table 2. Specifications of the considered cameras.

	AMICA	Proposed NAC	Rosetta NAC[8]
IFOV [μrad/px]	99.3	15.3	18.6
Field of View [deg]	5.83×5.69	0.9×0.9	2.2×2.2
CCD Format [px]	1,024×1,000	1,024×1,024	2,048×2,048
CCD pixel size [μm]	12	12	13.5
Focal Length [mm]	120	784	717
Aperture [mm]	15	75	87.5

Spectrometer The Argus 1000 IR Spectrometer has been selected for this mission as a COTS solution for asteroid spectroscopy. This spectrometer captures high-resolution observations with a 6 nm spectral resolution, and can observe wavelengths in the 1,000 to 2,500 nm range. Its field of view is 0.15 deg, satisfying the spatial resolution requirement of “a few decameters” at 10 km

Table 3. Propulsion Specifications.

	8-cm XiPS	µCAT
Thrust	2 - 14 mN	1 - 50 µN
$I_{sp}[s]$	2,000 - 3,000	2,500 - 3,000
Total Efficiency [%]	55.0	15
Mass [kg]	2.0	0.2
Total Input power [W]	100 - 350	2 - 14

altitude, where the FOV covers a 26×26 m footprint. The spectrum of the produced impact crater can also be analyzed on a low-altitude flyby.

Altimeter To improve the shape model scaling, gravity estimation flybys, optical navigation, and overall spacecraft safety, NEACO is equipped with a laser altimeter. The baseline for our instrument choice is the laser-altimeter flown on board Hayabusa-1,[11] which has a range from 50 m to upwards of 50 km.[12] This operational range allows the spacecraft to use the altimeter during all science phases of the mission. The altimeter has a mass of 3.56 kg and a power consumption of 22 W.[12]

Spacecraft Bus

Propulsion Preliminary trade studies identified the 8-cm Xenon Ion Propulsion System (XiPS)[13] as a viable SEP system for the considered class of small spacecraft. The 8-cm XiPS system follows a long series of flight-proven hardware. Since 1997, the larger 13-cm XiPS has been used for Boeing satellite stationkeeping; dozens of next-generation 25-cm XiPS have also flown.[14, 15] The new 8-cm XiPS incorporates improvements from both the 25-cm XiPS and 30-cm NSTAR. The latter is known for its success on NASA's Deep Space 1 and Dawn spacecraft.[14] Two thruster units will be able to provide the long required thrusting time, as the life-limiting components were tested in the 13-cm XiPS through more than 21,000 hours of operation.[15] For redundancy, two extra thrusters will be included for a total of four thrusters. NEACO is also equipped with six Micro-Cathode Arc Thrusters (µCATs) to allow for both hovering and reaction wheel desaturation operations. The µCAT has been flight tested and has a TRL of 7/8.[16] The pulsed plasma thrusters can also be used for attitude maneuvers and reaction wheel desaturation.[17] Table 3 lists the expected specifications for the 8-cm XiPS and the µCAT.

Power The power system is primarily designed towards the requirement of providing sufficient power to the Electric Propulsion System (EPS) during the cruise phase. Hence, the solar panels are sized to allow for continuous nominal EPS operation, without relying on batteries. In the event of attitude deviations, a secondary battery allows for 2.5 hr of continuous thruster use before the spacecraft enters a safe mode or phoenix mode (only spacecraft computer and radio receiver running). The power budget is summarized in Table 4; a detailed analysis is provided in the appendix.

Attitude Determination and Control Our ADCS package is based on Blue Canyon Technologies' Microsat Spacecraft sensor bundle[18] and RW1 reaction wheel systems.[19] This package provides a 1σ 0.002 deg three-axis pointing accuracy in addition to a one $1\ \mathrm{arcsecond/s}$ pointing stability over one second. These accuracy specifications ensure sufficient stability to provide the required image quality.

Communications and Data Handling The NEACO spacecraft is equipped with four patch antennas to receive communications from Earth, placed on different panels to enable full-sky coverage.

Table 4. Power Budget.

Mode	Power Draw [W]	Power Generated [W]	Margin [%]
Phoenix	1.84	N/A	N/A
Sleep	0.37	N/A	N/A
Cruise	356.17	395.92	10.04
Safe	26.17	395.92	93.39
Nominal	57.74	395.92	85.42
Payload Demo	35.66	395.92	90.99

The antennas have a gain of 9 to 11 dB and are able to transmit low-bandwidth telemetry data, such that two-way housekeeping communication is possible at all times, without requiring specific spacecraft attitudes. The spacecraft is equipped with an X-band transmitter for high-bandwidth communications, *i.e.*, the transmission of instrument measurements. Reflectarray panels are placed on the backside of the solar arrays to boost the X-band gain to 23 dB. This placement avoids the inclusion of communication-only deployables and reduces the mass and volume of the C&DH subsystem. As the resulting X-band transmission system has a beam width of approximately 10 deg, the spacecraft will usually need to rotate into an Earth-pointing attitude in order to transmit high-bandwidth data. In other words, instrument measurements and data transmission are unlikely to occur at the same time. This does allow the spacecraft to dedicate high power levels to the X-band system when in use. Note that onboard batteries allow for two hours of transmission at maximum power. The solar arrays will further extend this time in most geometries. The link budget available on page 3571 provides insight into the maximum available bitrate throughout the cruise and the arrival at HO_3. From the total 395 W provided by the solar rays, a maximum of 355 W can be dedicated to RF transmission. 70 W of RF power are thus transmitted to the RX channel assuming 20% of power conversion efficiency. The communication link budget can be found in the appendix, and was designed using the minimum power required at different Earth distances. The applied power can be increased to allow for faster data transmission. The budget makes use of the Deep Space Network (DSN) as a baseline, but can also use smaller ground stations such as Atlas to reduce operational costs.

Mass and Volume The spacecraft bus is designed to provide radiation shielding and sufficient surface area to stow the solar arrays, with dimension 50×50×70 cm. Significant margin is allocated for low-TRL components; high-TRL components are given a smaller margin. The internal volume available for system design and instrumentation is reduced to 40×40×60 cm after accounting for structural elements and solar arrays. All of the proposed asteroid facing instruments, *i.e.* the NAC (estimated maximum size corresponding the the Rosetta NAC), AMICA, spectrometer and altimeter, can fit on the 40×40 cm face with room to spare for thrusters. A summary of the mass budget with rounded values is provided in Table 5, with a more detailed budget provided in the appendix. Contingency percentages are actually selected based on the flight readiness of each individual component, and are note assigned by category. Note that the total mass budget refers to the wet spacecraft mass at launch.

Thermal NEACO's thermal subsystem maintains the spacecraft temperature within the allowable operating range during nominal operations. The subsystem is cold-biased, as the solar arrays provide sufficient heat when deployed. To achieve this cold-biasing, reflective coating and tapes are applied to the exterior bus. The applied silver Teflon tape has proven flight heritage from the MinXSS and QB-50 Challenger cubesats, and offers excellent thermal insulation.

Table 5. Mass Budget

Subsystem	Mass [g]	Contingency	Total Mass [g]
Structure	32,000	10%	35,200
Antennas	3,500	15%	4,000
Bus Components	64,000	7%	68,500
Payloads	22,700	20%	27,200
Fasteners	1,000	15%	1,150
Wires Harness	2,000	15%	2,300
Staking/Coating	1,000	15%	1,150
Total	126,200	12%	**139,500**
Allowed Mass			140,000
Remaining Mass			500

DESIGN PROCESS

Single vs Multiple Spacecraft

A great deal of consideration was given to multiple spacecraft options, but ultimately a single spacecraft configuration was selected. To account for radiation shielding needed in the two year trajectory, a single "mothership" option with a total mass of 140 kg and one or two deployable spacecraft included was considered. However, this option required the duplication of multiple flight systems, such as communications and power systems, that reduced available payload mass without a significant benefit in meeting mission goals. Multiple 140 kg spacecraft were also considered, but as shown in this proposal, all of the science goals can be met with a single 140 kg spacecraft solution. In either case, the addition of multiple spacecraft would simply serve to add increased cost, complexity, and mission risk without commensurate gains in science return.

Trajectory

The first step in the trajectory design process weighed high versus low-thrust propulsion and the use of gravity assists. The $C_3 \leq 0$ constraint combined with HO_3's relatively large inclination of $7.77°$ limits the use of classic, chemical propulsion. The smallest ΔV transfer identified required a total ΔV of 4.8 km/s and spanned 269 days. For a wet mass of 140 kg, this only allows between 12 and 42 kg of delivered mass for I_{sp} values between 200 and 400 s. The latter value would be difficult to provide, as 4.4 km/s would be needed for rendezvous at the end of the transfer. Cryogenic boil-off would reduce the achievable I_{sp} on this mission.

A chemical mission using lunar flybys was considered, but rapidly discarded. Besides imposing high navigation accuracies a few days post-launch, they can only be performed twice per month. Furthermore, the spacecraft would need a relative velocity to the Moon of approximately 4.3 km/s. At this high relative velocity, the Moon only provides a small turning angle, *i.e.*, the lunar flyby would not provide sufficient inclination change. A chemical mission using combinations of Earth and/or Venus flybys was also discarded, due to excessive ΔV requirements and/or times of flight.

Solar electric propulsion was selected as the choice low-thrust propulsion option. Solar sailing was initially investigated, but was not ultimately used due to challenges in dealing with SRP near HO_3. To that end, maximum payload trajectories were computed using the Evolutionary Mission Trajectory Generator (EMTG)[20] to complete the propulsion system trade study, identify launch and arrival windows, and determine the effectiveness of an Earth gravity assist. Having neglected the use of a lunar flyby, choosing to use the maximum allowable $C_3 = 0$ ensures that time and fuel are not wasted to depart Earth. Rendezvous with HO_3 facilitates insertion into the desired science orbit. Thrust and specific impulse were fixed to 0.9 mN and 2500 s, respectively, and a 90% duty cycle was assumed.

A grid of low-fidelity solutions was produced that begin with Earth's heliocentric position and velocity and are subject to two-body dynamics en route to HO_3. Low-thrust propulsion was modeled by impulsive maneuvers and Earth flybys by patched conics. Figure 6 details Earth gravity assist transfers around the nominal design point. Contour lines of wet mass are superimposed on the delivered mass to point out that maximum payload trajectories do not necessarily use the maximum allowable wet mass. Favorable transfer opportunities repeat approximately every six months. Direct transfers, *i.e.*, those without an Earth flyby, are detailed in Figure 7 and further justify the gravity assist option for improved delivered mass.

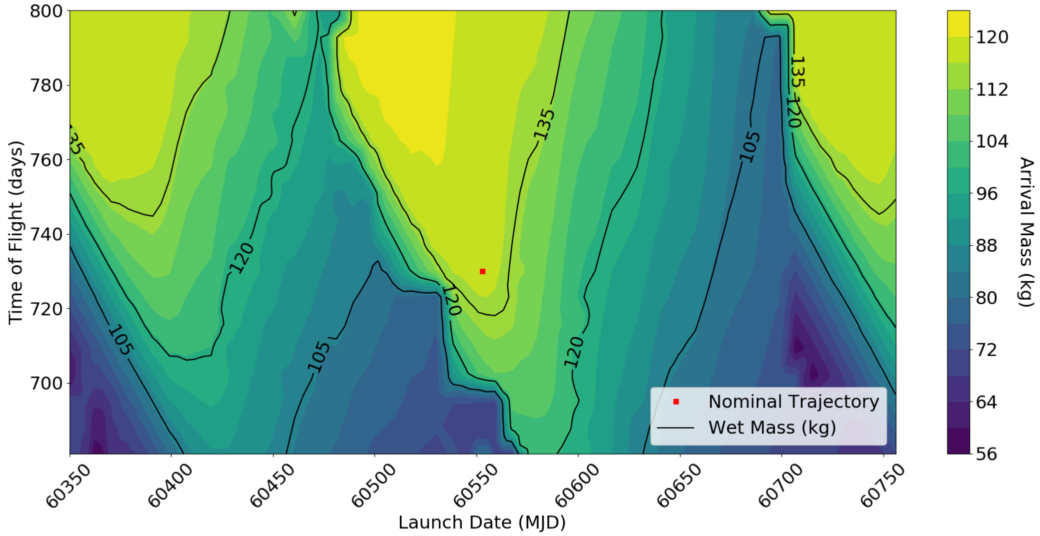

Figure 6. Maximum Payload Delivered to HO_3 With Earth Gravity Assist.

Resulting Trajectory A nominal trajectory was selected from the grid to fix the launch, Earth flyby, and HO_3 arrival dates. The next iteration improved the model fidelity and produced a fully integrated, continuous trajectory. Earth departure now begins in low-Earth orbit with coasting to Earth's sphere of influence. This initial segment was computed in GMAT. Similarly, the Earth flyby was numerically integrated with a 45-day inbound coast arc and 15-day outbound coast arc. These coast arcs are purposed for navigation, with the additional 30 days inbound for contingency maneuvers. Earth-centered dynamics included a 10×10 spherical harmonics expansion for the Earth and point mass perturbations from the Moon, Sun, Mars and Jupiter. Endpoints for the Earth departure and flyby segments and HO_3 arrival were connected in EMTG with finite-burn low-thrust replacing the impulsive maneuver approximation, with Earth gravity as a perturbing force. The resulting trajectory can be seen in Figures 2 and 8. This transfer takes exactly two years. It delivers 121.1 kg of dry mass, for a wet mass of 140 kg.

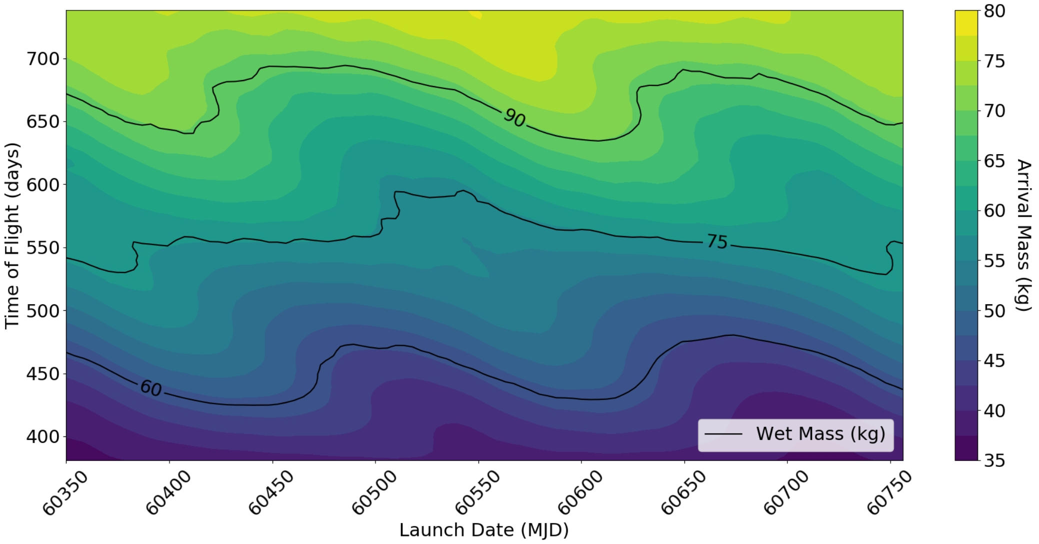

Figure 7. Maximum Payload Delivered to HO_3 With Direct Transfer.

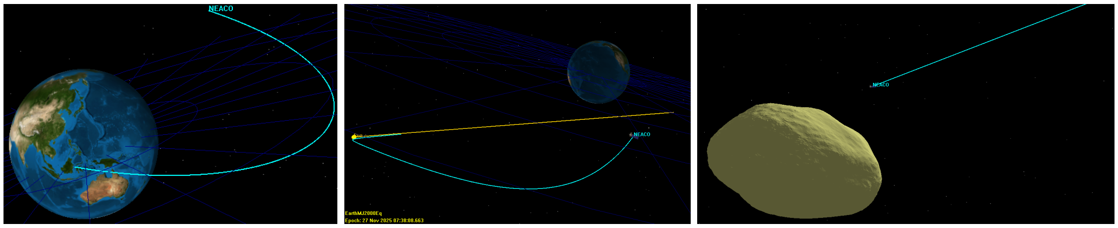

(a) (b) (c)

Figure 8. The nominal trajectory is visualized in GMAT with geocentric views of (a) Earth departure, (b) the 45-day coast to flyby periapse and (c) an HO_3-centered view of the final approach.

Acquisition

An important operational consideration for the mission is visual acquisition of the asteroid early enough to adjust the trajectory to the true asteroid position. While the uncertainty on the JPL Horizons ephemeris does not exceed 100 km during our interplanetary phase, it is still important to refine the trajectory as early as possible to prevent the need for drastic trajectory correction maneuvers. To estimate the earliest point at which the asteroid can be acquired for a given camera, we aim to achieve a signal to noise ratio (SNR) of 5 when taking an image. The first step in estimating SNR is calculating the apparent magnitude of HO_3 along the spacecraft's trajectory, based on the absolute magnitude of 24.3. Muinonen et al. give expressions for estimating the apparent magnitude of an asteroid,[21] the most important of which is the apparent magnitude expression in Equation 1.

$$m_V = H(\chi) + 5\,\log_{10} R\,R_{\odot,b} \tag{1}$$

Here, χ is the angle between the HO_3-Sun and HO_3-spacecraft lines and assumed to be $\geq 7.5°$, R and $R_{\odot,b}$ are the relative distance between the spacecraft and HO_3 and the Sun and HO_3 in AU, the slope parameter G is taken to be 0.15 (see Reference 21), and m_v is the apparent visual magnitude. The relation between apparent magnitude and flux, which is used to calculate the number of photons incident on the CCD, is given in Equation 2, where F is the flux of HO_3, F_0 is the reference flux for the visual band ($F_0 = 3640$ Jy).

$$F = F_0 \times 10^{-0.4 m_v} \tag{2}$$

Given that Jy is equal to 1.51×10^{-7} photons/s/m^2/($\Delta\lambda/\lambda$), and for visible wavelengths, $\Delta\lambda/\lambda = 0.16$, the number of visible band photons collected per second by a telescope with aperture $A = \pi\,\phi^2/4$ is

$$f = F\ \times 1.51 \times 10^7 \times \left(0.16\,\frac{\pi}{4}\,\phi^2\right) = 1.897521\ \times 10^6\ \times (F\,\phi^2) \tag{3}$$

where F is the flux measured in Jy and ϕ is the diameter of the telescope in meters. However, not all of these photons reach the CCD sensor due to optical considerations such as a secondary mirror shadowing the primary mirror (~10%), losses at each mirror reflection (~10%), and optical transmission losses (~30%). The CCD sensor also has a quantum efficiency, which gives the fraction of incident photons that are actually detected by the sensor. For this analysis we assume a quantum efficiency of 50% over all wavelengths to avoid integration. This results in an effective photon rate of $f^* = \zeta\,f = (0.9)^2\times, 0.7\times, 0.5\,f \simeq 0.28\,f$.

$$S/N = \frac{f^*\,t_e}{\sqrt{f^*\,t_e + f^*_{sky}\,t_e + Dt_e + N_r^2}} \tag{4}$$

To assess whether or not HO_3 is detectable, this photon rate must be compared to the background photons detected and sensor noise using the signal to noise ratio shown in Equation 4.[22] We assume that the night sky brightness is $\bar{m}_{V_{sky}} = 22$ mag/arcsec^2.[23] Hence, the number of sky photons collected by our camera per second and per arcsecond square is

$$\bar{f}_{sky} = \bar{F}_{sky}\ \times 1.51 \times 10^7 \times \left(0.16\,\frac{\pi}{4}\,\phi^2\right) = 1.897521\ \times 10^6\ \times (F_{sky}\,\phi^2) \tag{5}$$

with $\bar{F}_{sky} = 5.7690 \times 10^{-6}$ Jy/arcsec^2. The dark current D and read noise N_r are estimated using values provided by the Hayabusa AMICA[7] and Rosetta OSIRIS[8] reports when calculating SNR for the AMICA and proposed NAC respectively. Calculating SNR for our trajectory using Equation 4 shows that the AMICA can acquire the asteroid roughly 1.5 months prior to arrival, noting that it has a maximum exposure time of 178 seconds. The proposed NAC can acquire HO_3 at roughly three months before to arrival. Acquisition at three months gives plenty of time to adjust the trajectory, while acquisition at 1.5 months is a reasonable amount of time given that the uncertainty in HO_3's position is relatively low. The proposed NAC aperture of 75 mm could be reduced in order to save volume, which would move the acquisition time closer to arrival. However the larger aperture allows for faster exposure times during the science orbits, which reduces the ADCS requirements to achieve sharp images.

Relative dynamics

The system equilibrium points, hovering altitudes, and allowable mission operation phases are determined through a 3-body dynamics analysis. This analysis is crucial in dictating the allowable science phases for the mission.

Equations of Motion The equations of motion for a mass particle subject to the gravitational attraction of HO_3, solar gravity, and radiation pressure are derived as in Scheeres & Marzari.[24] The potential function is:

$$\mathcal{V}(\boldsymbol{r}) = \mathcal{U}(\boldsymbol{r}) + \frac{\mu_\odot - \beta}{\|\boldsymbol{r}_{b,\odot} + \boldsymbol{r}\|} + \frac{\mu_\odot + \mu}{r_{b,\odot}^2}\,\hat{\boldsymbol{r}}_{b\,\odot} \cdot \boldsymbol{r} + \boldsymbol{u} \cdot \boldsymbol{r} \tag{6}$$

where $\mathcal{U}(\boldsymbol{r})$ is the gravitational potential of HO_3, $\mu_\odot$ is the gravitational parameter of the Sun, $\beta = C_r\ (\Phi_\odot/c)\ AU^2/B$ is the SRP parameter, $\boldsymbol{r}_{b,\odot}$ is the position vector of HO_3 with respect to the Sun, $\boldsymbol{r}$ is the relative position vector of the spacecraft as seen from HO_3, and $\boldsymbol{u}$ is the input vector, i.e. the applied thrust. Furthermore, $\Phi_\odot = 1367$ W/m^2 is the solar irradiance, c is the speed of light, AU is the astronomical unit in meters, $C_r \simeq 1.3$ is the coefficient of reflectivity, and B is the mass-to-cross-sectional-area of the spacecraft, respectively.

We derive the equations of motion in a pulsating synodic reference frame $\mathcal{S}'$ centered at HO_3's center of mass, and rotating about the Sun with HO_3. For brevity, the final form of the equations is shown without derivation in Eq. (7):

$$\begin{cases} x'' - 2\,y' &= \dfrac{1}{1 + e\,\cos\nu}\,(\tilde{g}_x + \tilde{\beta} + 3\,x + \tilde{u}_x), \\ y'' + 2\,x' &= \dfrac{1}{1 + e\,\cos\nu}\,(\tilde{g}_y + \tilde{u}_y), \\ z'' + z &= \dfrac{1}{1 + e\,\cos\nu}\,(\tilde{g}_z + \tilde{u}_z). \end{cases} \tag{7}$$

in which:

$$\tilde{\boldsymbol{r}} = \frac{\boldsymbol{r}}{\epsilon\, r_{b\,\odot}} \quad \text{and} \quad \tilde{\boldsymbol{v}} = \frac{1}{r_{b\,\odot}}\left(\frac{\boldsymbol{v}}{\epsilon\,\dot{\nu}} - \tilde{\boldsymbol{r}}\, r'_{b\,\odot}\right) \tag{8}$$

are the normalized position and velocity coordinates of the spacecraft in the $\mathcal{S}'$ frame, and

$$\tilde{\boldsymbol{g}} = \frac{\epsilon^2\, r_{b,\odot}^2}{\mu}\,\boldsymbol{g} \quad \text{with} \quad \epsilon = \sqrt[3]{\frac{\mu}{\mu_\odot}} \tag{9}$$

is the normalized gravitational acceleration of the asteroid. In this expression, ν is the true anomaly of asteroid HO_3, and the heliocentric distance $r_{b\,\odot}$ of HO_3 is defined as:

$$r'_{b\,\odot} = \frac{r_{b\,\odot}^2\ e\,\sin\nu}{a(1 - e^2)} \quad \text{with} \quad r_{b\,\odot} = \frac{a(1 - e^2)}{1 + e\cos\nu} \tag{10}$$

Equilibrium Points and Periodic Orbits In order to better understand the system dynamics, we first ignore HO_3's eccentricity and determine the natural equilibrium points $\boldsymbol{x}^*$. We find two solutions, namely $x_{L_1} < 0$ and $x_{L_2} > 0$. The exact location on the x-axis depends on the value of the normalized SRP parameter $\tilde{\beta}$. Because of HO_3's shadow that is casted on the positive x direction, the second equilibrium point does not actually exist. For this reason, its use is not considered for proximity operations. Instead, we focus on the L_1 point and proceed with the inclusion of HO_3's eccentricity.

When $e \neq 0$, the L_1 equilibrium point becomes a periodic orbit where the spacecraft moves back and forth along the Sun-HO_3 line. The size of the periodic orbit depends on the mass-to-area ratio of the satellite and can be inferred from Figure 9, which shows the evolution of the same periodic orbit for a range of $\tilde{\beta}$ values.

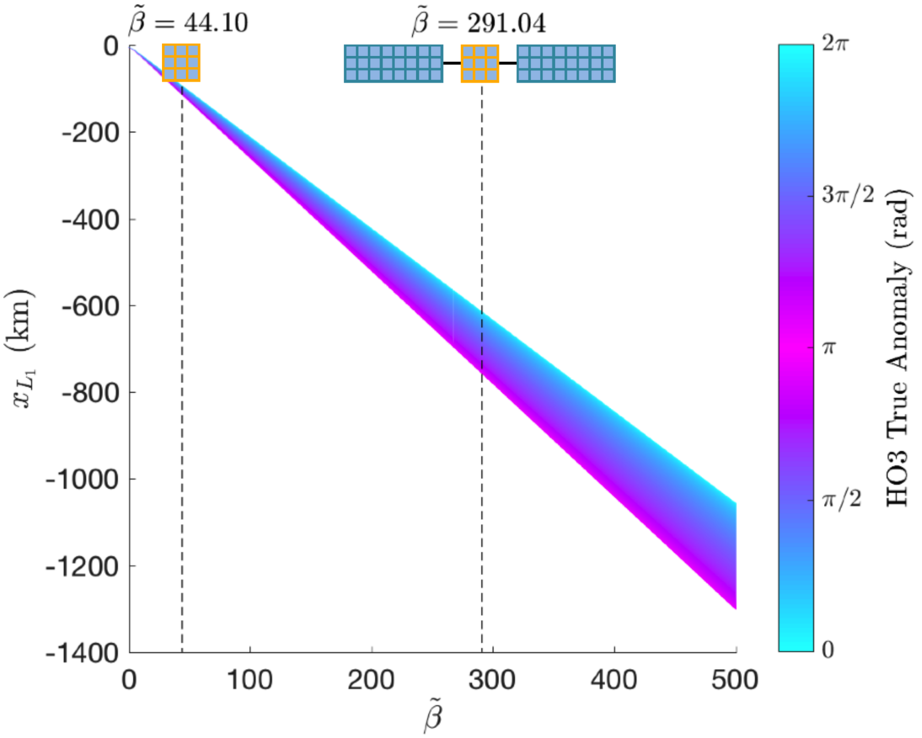

Figure 9. L_1 **periodic orbit for different** $\tilde{\beta}$ **values.**

When the solar arrays of NEACO are fully deployed and facing the Sun, the cross-sectional area of the spacecraft is roughly 1.65 m^2. Assuming that the delivered mass of the spacecraft is approximately $m = 120$ kg, the nominal value of the normalized SRP parameter is $\tilde{\beta} = 291.04$. This configuration allows for a periodic orbit with x-coordinates between -614 km and -757 km, as measured from the center of the asteroid. This periodic orbit is mildly unstable with unstable eigenvalue $\lambda_u = 1.0116$. This slow instability makes the L_1 periodic orbit particularly attractive for parking the spacecraft upon arrival and performing several subsystems performance checks before moving into science orbits at lower altitudes.

Spacecraft Hovering Figure 9 demonstrates that orbiting in a L_1 periodic orbit at a distance feasible for asteroid surface mapping is not possible, even when the the solar panels of NEACO are either folded or perpendicularly tilted ($\tilde{\beta} = 44.10$). Accordingly, there are no natural orbits that keep the spacecraft altitude fixed at the desired values. Instead, the team opted for a hovering approach and assessed the amount of ΔV required for each of the hovering phases proposed in the mission profile.

Thus, let $\boldsymbol{x}^* = \begin{bmatrix} x^*, & 0, & 0, & 0, & 0, & 0 \end{bmatrix}^T$ be the desired state of the satellite in the $\mathcal{S}'$ frame, where x^* is either 50, 10, or 6 km. From Eq. 7, it can be readily seen that $\tilde{u}_y = \tilde{u}_z = 0$, whereas:

$$\tilde{u}_x = -\tilde{\beta} - \tilde{g}_{x^*} - 3\,x^*. \tag{11}$$

Figure 10 displays the acceleration profiles required to counter the effect of gravity and solar radiation pressure at the different orbital regimes. As it can be seen, the difference between the 50, 10, and 6 km cases are fairly small: per month, 0.2143 m/s, 0.2122 m/s and 0.1982 m/s are required for respectively the 6, 10, and 50 km hovering phase. These values only provide an estimate of the

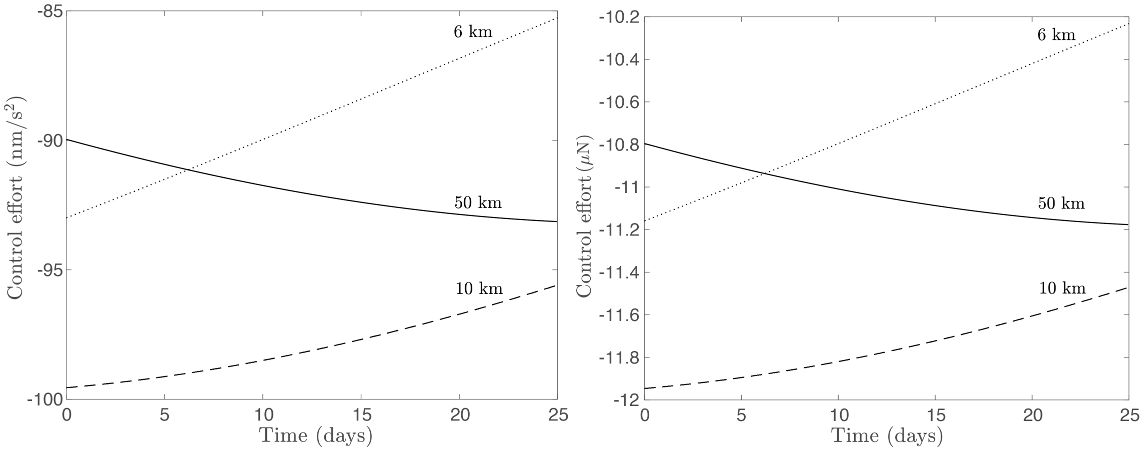

(a) (b)

Figure 10. Acceleration and thrusting profiles for different hovering altitudes.

order of magnitude of ΔV. Several factors must be included for the actual mission design. First, the thrusters should be stopped during scientific operation and communications. Second, navigation errors and mismodeled dynamics need to be included in the initial state and orbital propagation of the satellite. Nevertheless, considering that the maximum ΔV per month is 0.2143 m/s for hovering at 6 km (not planned for nominal mission operations), the team is confident that all of the hovering phases can be successfully completed with 1.5 to 2 m/s. These ΔV and thrust levels can be easily handled by the pulsed plasma thruster system envisioned onboard NEACO.

Terminator Orbits Terminator orbits allow for stable spacecraft operations close to the asteroid surface, where the dynamics are strongly perturbed by the irregular gravity field and solar radiation pressure. In such an environment, terminator orbits are frozen, and approximately circular, allowing for consistent resolution coverage of the asteroid surface.[25] Furthermore, such orbits remain clear of the asteroid shadow and thus provide constant maximum power availability to the solar arrays. However, for these orbits to be possible, the area of spacecraft with respect to the sun must be low. This requires the extended solar panels to be either gimbaled such that they remain perpendicular to the sun or retracted using specially designed joints. A properly designed terminator orbit naturally precesses with respect to the Sun and may survive for a long time, in spite of the highly perturbed dynamical environment of an asteroid.[25] Further optimization is possible by exploiting the attitude-orbit coupling resulting from strong solar radiation pressure effects.[26]

To investigate the applicability of terminator orbits to the NEACO mission, a Monte Carlo analysis is performed. In this analysis, orbit simulations are performed with uncertainties on the asteroid pole orientation, asteroid mass, SRP parameter β, and the initial spacecraft state shown in Table 6. Table 7 provides results on the most critical terminator orbit, *i.e.*, the orbit with semi-major axis $a = 150$ m that is necessary in the event of a NAC failure, when such a low altitude is necessary for the AMICA camera to satisfy the high-resolution imaging requirements. The table includes the shortest failure time (SFT), average failure time (AFT), and longest failure time (LFT). These results show that this orbit carries a notable risk, with a 13% chance of impacting the asteroid. In the worst impact case, impact occurs after only two days. Simulations for orbits with semimajor axes of 200 m and 250 m were also run, with the most safe orbit in terms of impact probability appearing to be the 250 m case with a 0.7% chance of impact and SFT of 9 days. For these low-altitude terminator orbit to be included in the spacecraft operations, extensive analysis with accurate gravity and SRP models would thus be required. These can be obtained during the early science operations at the hovering positions.

Table 6. Monte Carlo input errors. $\mathcal{U}_x([a,b])$ denotes a uniform distribution for the continuous random variable $x \in [a,b]$.

Error Source	Variable	Uncertainties
HO_3 attitude	3-1-3 set of Euler angles: $\theta_1, \theta_2, \theta_3$	$\mathcal{U}_{\theta_1}([0, 2\,\pi])$ $\mathcal{U}_{\theta_2}([0, \pi])$ $\mathcal{U}_{\theta_3}([0, 2\,\pi])$
HO_3 initial true anomaly	ν_0	$\nu_0 = \mathcal{U}([0, 2\,\pi])$
HO_3 gravitational parameter	μ	$3\sigma_\mu = 0.10\,\mu$
S/C SRP parameter	β	$3\sigma_\beta = 0.10\,\beta$
S/C initial position error	$\boldsymbol{r}_0$	$1\sigma_{r_0} = 1$ m
S/C initial velocity error	$\boldsymbol{v}_0$	$1\sigma_{v_0} = 1$ mm/s

Table 7. Monte Carlo Simulation for Terminator Orbit with 150 m semi-major axis.

	Chance	SFT [d]	AFT [d]	LFT [d]
Impact	13.10%	2.01	13.87	35.81
Escape	2.70%	7.54	10.13	17.54
Success	84.20%	-	-	-

Gravity Estimation

The flybys described in the mission concept are designed to estimate the mass of HO_3 by observing the passage time between two mirroring true anomaly angles in a hyperbolic trajectory. This method, developed by Takahashi and Scheeres[27] and denoted as the $\mu_{||}$ parameter estimation method, observes the difference between the expected passage time when no asteroid gravity is present and the actual time of passage when passing under the influence of HO_3's gravity. The very small mass assumed for HO_3 (derived from given volume and density values), with a sphere of influence at $r_{SOI} = 0.242$ km, requires these close flybys in which the effect of the asteroid's gravity can be observed and measured.

Table 8 presents the five flybys trajectory parameters and expected performances. The parameters are the incoming hyperbolic velocity V_∞, the magnitude of targeted B-plane crossing vector b_∞, the radius of periapse b_p, the expected passage time t (under the influence of HO_3's gravity), and the expected 3-sigma error in HO_3 gravitational parameter estimation σ_μ. For all flybys, a hyperbolic eccentricity of $e = 10$ is defined and the passage is defined between 20 km before and after the B-plane crossing, which translates to the income/outgoing true anomaly angle values of around 85 deg.

Note that in Table 8 that the expected gravitational parameter estimation error after the fifth and final flyby is substantially smaller than the required 10% error. This added tenfold factor is put in place to account for the lack of SRP consideration in the $\mu_{||}$ method. Figure 11 shows the dominant accelerations felt by the spacecraft near HO_3 in the HO_3 frame. Note that the gravity acceleration decreases compared to the fixed SRP acceleration for both the maximum and minimum SRP configurations. At the minimum distance flyby ($b_p = 0.6$ km) the maximum SRP acceleration is in the same order of magnitude as HO_3's gravity. Thus, even though the $\mu_{||}$ does not account for

Table 8. Mass estimation flybys.

Flyby No.	V_∞ [m/s]	b_∞ [km]	b_p [km]	t [hr]	$3\sigma_\mu$ [%]
1	0.5	2.1	2.0	11.58	2641.5
2	0.4	1.6	1.5	12.61	624.6
3	0.3	1.1	1.0	10.12	213.6
4	0.2	0.9	0.8	17.75	14.9
5	0.1	0.7	0.6	38.23	0.87

SRP, the 10% error mass estimation is expected. Figure 12 shows the expected estimation error as a function of V_∞ and b_p, the last flyby values are marked on the surface.

As mentioned, the main measurement type for the $\mu_{||}$ method is the true anomaly angle and flyby time. The time counting error is considered negligible in the time scales presented and thus the true anomaly error is the main source of measurement error. This error is based on the accuracy of the measured pointing vector between spacecraft and asteroid and is defined $\sigma_\nu = 10^{-4}$ rad. The initial state of each flyby and the periapse crossing distance estimation errors are also assumed to be negligible based on orbit determination schemes standard for deep space missions.

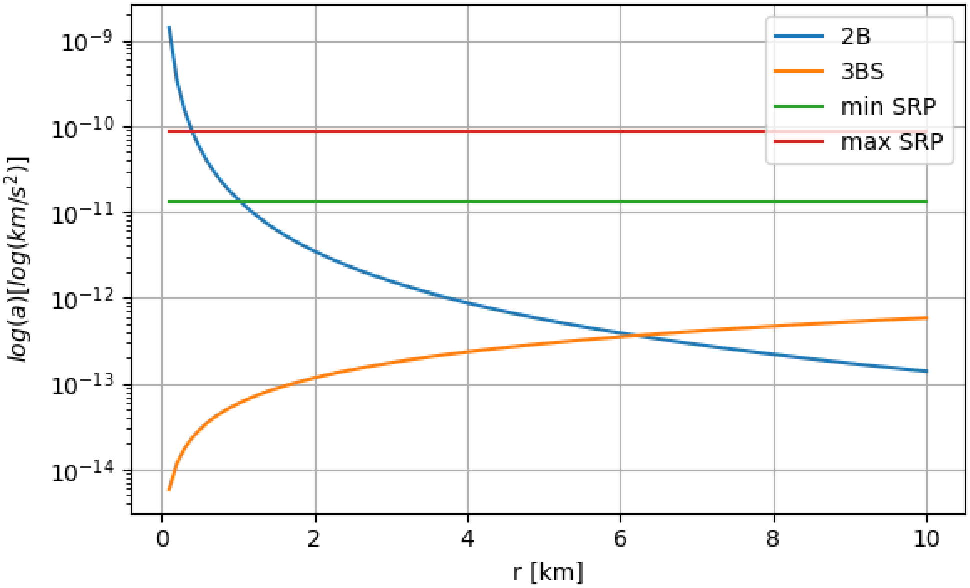

Figure 11. Acceleration magnitudes in the HO_3 environment.

Instrument Selection

Optical Imaging vs. Lidar vs. Radar Remote sensing instruments are either considered to be active or passive sensors, depending on whether or not they carry their own illumination source. Two major types of *active* sensors with flight heritage are available: radars and lidars. Radars operate over a large frequency band in the RF spectrum ranging from 3 MHz (low HF band) up to 300 Ghz (high micrometer band). Synthetic Aperture Radar (SAR) is the method of choice for reconstructing topography from a varying observation geometry, and has been in particular used by the Cassini mission to image the surface of Saturn's moon Titan.[28] However, typical SARs power requirements are nearly an order or magnitude beyond what our platform can provide. In addition,

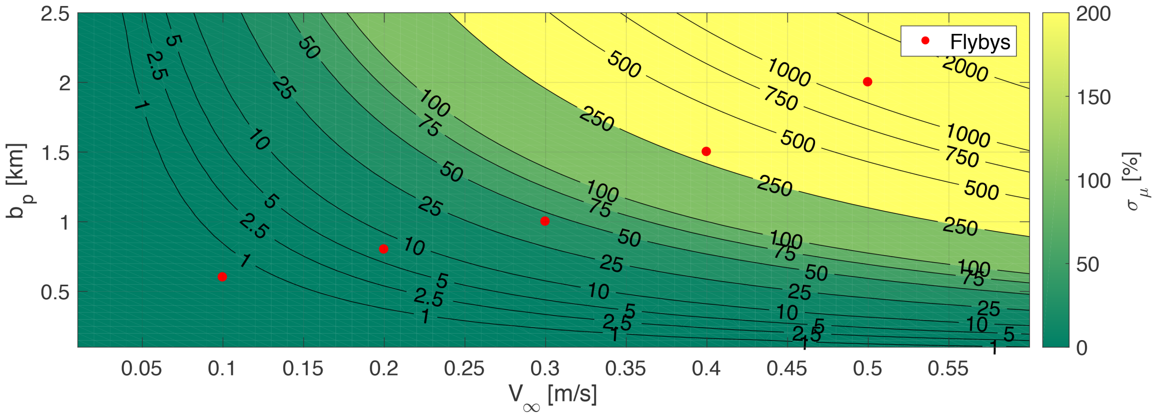

Figure 12. $\mu_{||}$ estimation errors.

the necessary matching between a SAR's antenna dimensions and its operating wavelength makes its integration on board of a volume-limited 140 kg spacecraft extremely challenging. It is also worth noting that the SAR data products require intense processing before they can be utilized.

Contrary to radar, lidar operates around the optical region of the RF spectrum. To date, only three major missions (Hayabusa-1, Hayabusa-2, and OSIRIS-REx) carried a lidar in their instrument suite, operating at 1064 nm.[11] They produce discrete point clouds representative of the topography of the observed scene. Due to their higher position in the RF spectrum, they have much smaller dimensions than radar systems and are also nearly insensitive to relative motion between the image shape and the instrument.[29]

Lidars also have limiting factors. First, they require significant amounts of power to operate. The GoldenEye flash lidar and OLA scanning lidar onboard OSIRIS-REx require respectively 50 and 60 W.[29,30] Second, current lidar can operate up to ranges around 10 km due to the reflected power falling under detection thresholds. In addition, reflected power and hence operating range will most likely be further reduced because of the low albedos typical for planetary bodies such as asteroids.[31]

As pointed out in the "Terminator Orbits" section on page 3559, HO$_3$'s terminator orbits have radii that are within the lidar operating range. Yet, the required power to operate the lidar system can only be provided with fully-deployed solar arrays. The high area-to-mass ratio, and thus high SRP, requires smaller terminator orbit radii. Operating so close from HO$_3$ would demand a high confidence in the dynamical environment. This high risk level would only be acceptable late into the mission. That is, compared to optical instruments, lidar sensors can only be operated over a much smaller altitude range and after much delay. Active sensors thus appear at best impractical from a mass, power and volume perspective. On the other hand, *passive* optical instruments such as the AMICA and the proposed NAC sensors fulfill the imaging requirements as shown on page 3549. In addition, they do so from much greater distances than lidar sensors, have lower volume, mass and power requirements than both radar and lidar instruments and are lower-risk systems due to their flight heritage.

Optical Imaging and Analysis One of the main driving requirements in the optical imaging instrument selection is the instantaneous field of view (IFOV). This parameter dictates the distance at which a given instrument can meet the various resolution requirements outlined in the competition guidelines. A wide array of instruments were considered as candidates for inclusion in the NEACO mission. Plots similar to figure 5 were generated with candidate cameras to allow iterative selection as the orbit selection and payload mass were narrowed down. The NAC IFOV was selected to allow operational and scientific goals to be met from relatively safe altitudes. The NAC IFOV satisfies the required resolutions of 1 m and 1 cm/px at altitudes respectively of 50 km and 600 m, as opposed to the 10 km and 100 m altitudes required for the AMICA camera that serves as a backup.

Given that so many science goals and operational needs are met using an optical camera, the inclusion of multiple cameras is required for redundancy purposes. As the main NAC camera has significant mass and volume requirements due to its large focal length and aperture, the smaller AMICA camera with wider FOV was selected as secondary camera. The AMICA, flown on the Hayabusa-1 spacecraft, is able to satisfy the mission goals in the event of a NAC failure. In nominal mission operations, AMICA's wider FOV may help contextualize NAC images of HO_3 at altitudes lower than 6 km, where the asteroid fills NAC's field of view. AMICA also has has a filter wheel that may provide regional spectral information of the surface, though its resolution is far lower than the Argus spectrometer.

Resolved images of HO_3's surface collected by the cameras will be processed by means of stereophotoclinometry. Provided with an arbitrary large number of overlapping optical images, SPC produces an ensemble of landmark maps (L-maps) that are small digital albedo and elevation maps. Each L-map is thus a three-dimensional "tile" of the small body's surface.[32] These L-maps can then be used as navigation features or as the building blocks for a Global Topography Model (GTM). SPC is very robust to varying lighting conditions, image resolution, and angular separation. For instance, the Rosetta team reported a compatibility of SPC with surface-normal-to-camera angles (emission angles) up to 85 ° and phase angles ranging from nearly 0° to 160 °.[33] This method is thus suitable to an iterative reconstruction of HO_3's shape .

Altimeter An altimeter similar to the instrument flown onboard Hayabusa-1 is included in our instrument package, as multiple mission goals directly benefit from it. First, the determination of HO_3's gravitational parameter is dependent upon knowledge of the spacecraft state along the fly-by trajectory. As pointed out in the "Gravity Estimation" section on page 3548, the reconstruction of this trajectory can be greatly improved if range measurements are available in complement with shape-model based optical navigation techniques (OPNAV). Second, the reconstructed shape model as well as the OPNAV solution are only known up to a scaling factor. That is, the shape size and the separation between the imager and the shape are mutually indistinguishable. For large bodies such as Eros, the gravitational pull is sufficient to make this scaling factor observable in Doppler measurements when the spacecraft is undergoing ordinary orbital motion.[32] For smaller bodies like Itokawa, specific free-fall Doppler-tracked trajectories must be instantiated in order to recover the scaling factor. For even smaller bodies like HO_3, it is envisioned that this would be even harder to schedule and accomplish. On the other hand, an altimeter would provide an unambiguous range measurement regardless of the orbital regime or the potential perturbations caused by maneuvers. In addition, contingencies arising during the proximity operations (such as imminent impact or escape) could be more easily detected and dealt with the altimeter than without.

Spectrometer Asteroid 2016 $H0_3$ is most likely a Q- or S-type asteroid. Therefore, it is likely to be similar to ordinary chondrite meteorites. This characterization comes from two distinct absorption bands in the asteroid's spectra profile, one at 1 μm band and one at 2 μm band.[34] General trends of S-Type and Q-Type asteroid spectra can be seen in Figure 13(a).

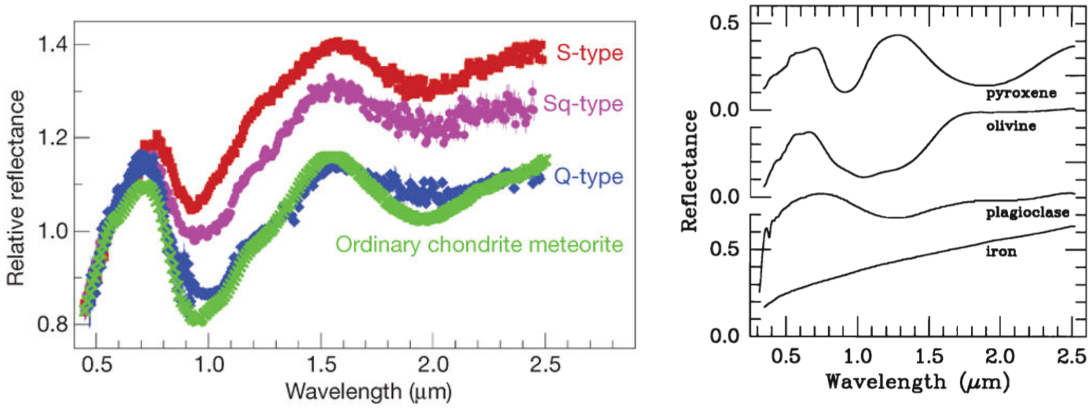

(a) (b)

Figure 13. (a) Reflectance spectra properties of ordinary chondrite meteorites compared with asteroids grouped according to taxonomic types by Binzel et al.[35] (b) Reflectance spectra of pure minerals by Nelson et al.[36]

The primary goal when understanding these spectra is determining some of the components of the surface. For S- and Q-type asteroids, this involves understanding the compositions of their closest meteorite counterpart, the chondrite meteorites.[34] These meteorites are comprised of pyroxene, olivine, and metals. Therefore, when determining the composition of H03 2016, it is important to compare with the mineral spectra shown in Figure 13(b). Table 9 also shows how the characteristics of the spectrum relates to mineral content.

Table 9. Mineralogical Significance of Spectral Parameters adapted from Gaffey et al.[37]

Spectral Parameter	Mineralogical Implications
1 μm and 2 μm band area ratio	Olivine-pyroxene abundance ratio
1 μm band position	Ca^{2+} content of pyroxene Olivine-pyroxene abundance ratio Fe^{2+} olivine content
2 μm band position	Fe^{2+} pyroxene content Ca^{2+} pyroxene content
1 μm band depth	Fe^{2+} olivine/pyroxene content Mafic mineral particle size Abundance of absorbing mineral phase
Spectral slope	NiFe metal content Olivine abundance Agglutinate abundance

The key characteristics of Q- and S-type asteroids are absorption bands at the 1 μm and 2 μm in the reflectance spectra. Therefore, it is crucial that those two bands are included in the spectrometer's wavelength range. Furthermore, the minerals most likely to be observed have feautures in wavelengths between 0.5 μm an 2.5 μm. Therefore, it is of medium priority to include those spectra as well. This led us to select the Argus Space Grade IR Spectrometer. The spectra of this instrument ranges from 1 μm to 2.5 μm as part of its extended package which not only encompasses both the 1 μm and 2 μm absorption bands, but also the upper portion of the medium-priority spectrum.

ADCS Package Selection

The Blue Canyon Technologies FlexCore ADCS package was picked based on the attitude control requirements imposed by the acceptable levels of motion blur when using optical cameras during science operations. To determine the acceptable levels, one can at first assume that the spacecraft has a non-zero angular drift $\boldsymbol{\omega}_D$ rate about the asteroid spin axis $\hat{\boldsymbol{\omega}}_T$. The relative attitude set-up for this one dimensional representation is visualized in Figure 14. It shows a simplified pinhole camera at a distance r from the target. The target is modeled as a rotating rod of length R_T. This low-fidelity model helps determining a worst-case scenario in terms of relative motion.

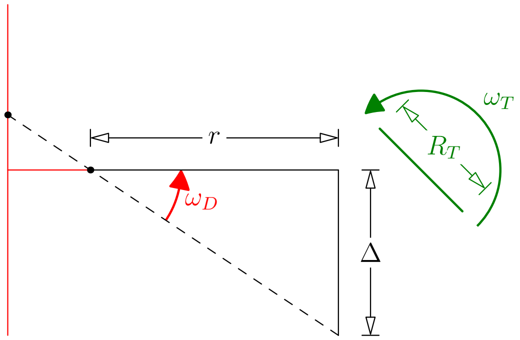

Figure 14. Depiction of relative attitude components used to determine pointing requirements.

Over a short time interval δt, a point initially aligned with the line of sight drifts by Δ:

$$\Delta \simeq \delta t(\omega_T R_T + \omega_D r) \tag{12}$$

In the vicinity of HO$_3$, exposure times around one second have a signal to noise ratio orders of magnitude above the detection threshold of $S/N = 5$ (see "Acquisition" section on page 3555). Over such a short time, the approximations used in this derivation remain valid. Zero-motion blur is achieved when the displacement Δ is exactly zero. That is, $\omega_D^* = -\frac{\omega_T R_T}{r}$. The two drift rates exactly equating the maximum allowable drift rate are $\omega_{D,+} = \omega_D^* + \frac{\Delta}{r\Delta t}$ and $\omega_{D,-} = \omega_D^* - \frac{\Delta}{r\Delta t}$. In order to satisfy the lit surface mapping requirements, we must have $\Delta < 1$ m. The objective is to meet this requirement during the $r = 50$ km altitude hovering phase. As a result, the maximum allowable angular velocity drift for the 1-meter resolution over one second is:

$$\Delta\omega_{max} = \frac{\omega_{D,+} - \omega_{D,-}}{2} = \frac{\Delta}{r\Delta t} = 2 \cdot 10^{-5} \text{ rad} = 0.0011 \text{ deg} = 4.12 \text{ arcsec/s} \tag{13}$$

The Blue Canyon XB Microsat package's pointing stability is rated at ±1 arcsec/s*. Since our analysis was conducted for a worst-case scenario where the angular displacement is maximum, this ADCS package appears to suit the needs of the mission. A more detailed analysis would need to account for wheel saturation and coupling between attitude knowledge and the attitude control system over all mission phases.

The nominal slew rate evaluates to $|\omega_D^*| = 3.88 \cdot 10^{-6}$ rad/s $= 0.00022$ deg/s $= 0.8$ arcsec/s. Since the torque discretization of the reaction wheels is limited, the pulsed plasma thrusters could be used in complement so as to achieve this extremely low rotation rate.

---

*`http://bluecanyontech.com/wp-content/uploads/2017/07/DataSheet_XBSpacecraft_09.pdf`

Strength Characterization

The measurement of an asteroid's strength provides scientific insight at several levels. First, planetary accretion in the early Solar System occurred through the collision of planetesimal bodies; asteroids are thought to be remnants of this primordial planetesimal population.[5] Measurements of their strength may therefore improve our understanding of the accretion processes that dominated the early Solar System. Second, the design robustness of a kinetic impactor for planetary defense purposes is improved with accurate knowledge of its target's internal structure and strength as well as providing in situ data on the momentum transfer efficiency.[38,39] Finally, methods to extract resources from asteroids, which have the potential to significantly decrease the cost of spaceflight, must be tuned towards the surface properties of their target.[40]

When discussing asteroid strength, a distinction is made between the cohesive, tensile, and compressive strength of a body. The cohesive strength refers to Van der Waals forces between small grains that make up the unconsolidated regolith found on many asteroids and comets.[41] Due to HO_3's fast rotation rate, the net surface force points outwards across almost all of the asteroid's surface. Only near the rotation poles could we find regions of approximately 1 meter radius where the net slope is small enough to allow loose particles or rocks to exist. If the cohesion between regolith grains and the surface is high, this region could be slightly larger. However, any precession/nutation in the asteroid rotation would catastrophically disrupt the region's stability. Although the cohesive strength could theoretically be inferred by measuring the maximum slope at which loose particles are found,[42] the expected absence of such particles renders this measurement improbable.

The tensile strength of a body refers to its resistance to tensile forces, and manifests itself mostly through the size and slope of overhangs on the asteroid surface. By examining cracks and cliffs with landslides, the tensile strength of a surface can be estimated. This was done for comet 67P/C-G during the Rosetta mission.[43] However, as mentioned before, loose objects such as debris from overhanging cliffs cannot exist on the surface of HO_3. This will make it difficult, if not impossible, to determine if a surface feature is a failed overhang/cliff or simply part of the natural shape in which HO_3 formed. A measurement of this 'critical' tensile strength is thus also expected to be improbable. At best, a lower bound on the tensile strength can be constructed from accurate gravity, shape, and rotation models by estimating the internal stresses in the asteroid, which result primarily from its fast rotation rate.

Finally, the compressive strength of a body represents its resistance to compressive forces. This strength can be measured by penetrating or breaking the asteroid surface. Although this could be achieved using a lander equipped with a drill, such a system would need to be anchored to HO_3's surface to resist the centrifugal accelerations of its rotation. The complexity and mass of such a system would exceed this mission's budgets. An alternative method for measuring the compressive strength is through the use of a kinetic impactor. This technique will be demonstrated by the Hayabusa-2 mission, where a 2.5-kg impactor is planned to be launched into the surface of asteroid Ryugu using a 4.5-kg high-energy HMX explosive.[5] The impactor assembly (called Small Carry-on Impactor, or SCI), has a total mass of 18 kg and is released from the main spacecraft prior to a timer-based detonation. A scaled-down version of this assembly can be included in our mission.

To determine a preliminarily size of the impactor assembly, we make use of the work by Poelchau et al.,[44] who performed experiments with small spheres fired into sandstone at high velocity. Although the composition of HO_3's surface is unknown, we selected sandstone as an analogue as this sedimentary rock is some of the weakest consolidated rock found on Earth. Furthermore, the sandstone targets used by Poelchau et al. have a density of 2.01 to 2.30 g/cm^3, which is similar to HO$_3$'s estimated density of 2.00 g/cm^3. They combine their experimental results with the theoretical work by Holsapple[45] and fit cratering laws to the observed sandstone craters. In this, the excavated crater volume V is determined as function of the impactor properties including its impact velocity v_i, and various surface properties including its strength Y. We can use this relationship to select an impactor size and velocity that creates a sufficiently large crater. Here, we choose to create a 1-meter-diameter crater as an order-of-magnitude preliminary design. This size should be sufficiently large to make post-impact detection by the mothership relatively easy, yet small enough that catastrophic disruption of the monolithic 100-meter asteroid is not a risk. Fixing the launch velocity to match the v_i =2.0 km/s used by Hayabusa-2's SCI, we find that a 0.500 kg copper impactor would create this crater when impacting a consolidated surface with density 2.0 g/cm^3 and strength 10 MPa. The corresponding scaled HMX explosive mass is 0.880 kg, with a total scaled assembly mass of approximately 2.2 kg. Assuming a crater depth-diameter ratio matching that of Poelchau et al., the corresponding crater depth will be 20 cm, with a total excavated mass of 170 kg.

Although it is difficult to estimate the expected surface strength of HO$_3$, the nominal value of $Y = 10$ MPa is a conservative estimate given that the Philae lander discovered a hard layer with $Y = 2 - 4$ MPa underneath the regolith of comet 67P/C-G.[46] We note that the weakest sandstone tested by Poelchau et al. has a compressive strength of approximately 50 MPa. The nominal impactor assembly would create a crater with a diameter of 67 cm in such a surface. This size remains well above the minimum resolution observable by the proposed hardware. Similarly, if the surface is much weaker with a compressive strength of only 1 MPa, the corresponding crater size would be 186 cm. The kinetic energy of the 0.5 kg impactor launched at 2.0 km/s remains approximately four orders of magnitude below the energy level required for catastrophic disruption, even when taking into account more dramatic scaling effects.[47]

CONCLUSIONS

The NEACO mission proposes to perform an elementary investigation of asteroid 2016 HO$_3$ using a single SmallSat spacecraft on a low-thrust SEP transfer trajectory. Pulsed plasma thrusters allow for hovering and maneuvering in proximity of the asteroid. The spacecraft is equipped with two optical cameras, a spectrometer, a laser altimeter, and an explosive impactor assembly. This instrument suite allows NEACO to resolve the asteroid shape, estimate its mass, perform mapping and spectroscopy of the surface, and measure the strength of this small, fast-rotating, near-Earth asteroid.

ACKNOWLEDGMENTS

Thanks to Dr. Jay McMahon, Dr. Simon Tardivel, Dr. Masatoshi Hirabayashi, Dr. Jason Leonard, and Dr. Jacob Englander for consulting with our team to give general advice. Also thanks to Dr. Ann Dietrich and Dr. Trevor Bennett for consulting with the team while still students at CU Boulder. Finally, thanks to Ph.D. student Luke Bury for his input as well. This work was supported by a NASA Space Technology Research Fellowship.

REFERENCES

[1] GMAT, General Mission Analysis Tool, Software Package, Version R2016a, NASA Goddard Space Flight Center, Greenbelt, MD, 2013.

[2] "Estimating the Mass of Asteroid 433 Eros During the NEAR Spacecraft Flyby," *Science*, Vol. 285, No. 5427, 1999, pp. 560–561, 10.1126/science.285.5427.560.

[3] S. Broschart, S. Bhaskaran, J. Bellerose, A. Dietrich, D. HAn, R. HAw, N. Mastrodemos, W. Owen, B. RUsh, and D. Surovik, "Shadow Navigation Support at JPL for the Rosetta Landing on Comet 67P," *26th International Symposium on Space Flight Dynamics*, Matsuyama, 2017.

[4] C. D. Jackman, D. S. Nelson, L. K. Mccarthy, T. J. Finley, A. J. Liounis, K. M. Getzandanner, and P. G. Antreasian, "Optical Navigation Concept of Operations for the Osiris-Rex Mission," No. Code 595, 2018, pp. 1–18.

[5] T. Saiki, H. Sawada, C. Okamoto, H. Yano, Y. Takagi, Y. Akahoshi, and M. Yoshikawa, "Small carry-on impactor of Hayabusa2 mission," *Acta Astronautica*, Vol. 84, 2013, pp. 227–236.

[6] D. Scheeres, D. Durda, and P. Geissler, "The fate of asteroid ejecta," *Asteroids III*, 2002, pp. 527–544.

[7] M. Ishiguro, R. Nakamura, D. J. Tholen, N. Hirata, H. Demura, E. Nemoto, A. M. Nakamura, Y. Higuchi, A. Sogame, A. Yamamoto, K. Kitazato, Y. Yokota, T. Kubota, T. Hashimoto, and J. Saito, "The Hayabusa Spacecraft Asteroid Multi-Band Imaging Camera: AMICA," *Icarus*, Vol. 207, June 2010, pp. 714–731.

[8] H. U. Keller, C. Barbieri, P. Lamy, H. Rickman, R. Rodrigo, K.-P. Wenzel, H. Sierks, M. F. A'Hearn, F. Angrilli, M. Angulo, *et al.*, "OSIRIS – The Scientific Camera System Onboard Rosetta," *Space Science Reviews*, Vol. 128, Feb 2007, pp. 433–506, 10.1007/s11214-006-9128-4.

[9] H. Jin, J. Lim, Y. Kim, and S. Kim, "Optical design of a reflecting telescope for cubesat," *Journal of the Optical Society of Korea*, Vol. 17, No. 6, 2013, pp. 533–537.

[10] N. Bosanac, S. Do, H. Y. Wen, and A. Wicht, "A general purpose astronomy small satellite: an approach to low-cost space telescope design using space-qualified ground telescopes," SPIE, 2010.

[11] K. Tsuno, E. Okumura, Y. Katsuyama, T. Mizuno, T. Hashimoto, M. Nakayama, and H. Yuasa, "Lidar on Board Asteroid Explorer Hayabusa," *Manufacturing Engineering*, Vol. 2006, No. June, 2006, pp. 27–30.

[12] T. Mukai, H. Araki, T. Mizuno, N. Hatanaka, A. Nakamura, A. Kamei, H. Nakayama, and A. Cheng, "Detection of mass, shape and surface roughness of target asteroid of MUSES-C by LIDAR," *Advances in Space Research*, Vol. 29, No. 8, 2002, pp. 1231–1235.

[13] W. G. Tighe, K. Chien, J. Ahn, J. Hurtado, E. Solis, and R. Spears, "Update on the XIPS 8-cm Thruster Prototype," *44th AIAA/ASME/SAE/ASEE Joint Propulsion Conference & Exhibit*, July 2008.

[14] D. Manzella, "Low Cost Electric Propulsion Thruster for Deep Space Robotic Missions," *2007 NASA Science Technology Conference*, June 19-21 2007.

[15] W. Tighe, K. Chien, and R. Spears, "XIPS Ion Thrusters for Small Satellite Applications," *21st Annual AIAA/USU Conference on Small Satellites, SC07-III-11*, August 13-16 2007.

[16] E. Agasid, R. Burton, R. Carlino, G. Defouw, *et al.*, "Small Spacecraft Technology State of the Art," tech. rep., Technical Report NASA/TP–2015, 2015.

[17] M. L. McGuire and R. M. Myers, "Pulsed plasma thrusters for small spacecraft attitude control," 1996.

[18] "XB Spacecraft Buses Specifications," tech. rep., Blue Canyon Technologies.

[19] "Attitude Determination & Control. FlexCore package datasheet,"

[20] J. A. Englander and B. A. Conway, "Automated Solution of the Low-Thrust Interplanetary Trajectory Problem," *Journal of Guidance, Control, and Dynamics*, Vol. 40, January 2017, pp. 16–26.

[21] K. Muinonen, I. N. Belskaya, A. Cellino, M. Delbò, A.-C. Levasseur-Regourd, A. Penttilä, and E. F. Tedesco, "A three-parameter magnitude phase function for asteroids," *Icarus*, Vol. 209, No. 2, 2010, pp. 542–555.

[22] Photometrics, "Keep the Noise Down! Low Noise: An Integral Part of High-Performance CCD (HCCD) Camera Systems," tech. rep., 2010. https://www.photometrics.com/resources/technotes/pdfs/snr.pdf.

[23] C. Barbieri, S. Fornasier, I. Bertini, F. Angrilli, G. Bianchini, S. Debei, M. De Cecco, G. Parzianello, M. Zaccariotto, V. Da Deppo, *et al.*, "First Results from the Wide Angle Camera of the ROSETTA Mission.," *Memorie della Societa Astronomica Italiana Supplementi*, Vol. 6, 2005, p. 28.

[24] D. J. Scheeres and M. F., "Spacecraft Dynamics in the Vicinity of a Comet," *Journal of the Astronautical Sciences*, Vol. 50, No. 1, 2002, pp. 35–52.

[25] D. J. Scheeres, *Orbital Motion in Strongly Perturbed Environments*. Springer-Verlag Berlin, 2012.

[26] S. Shota Kikuchi, K. C. Howell, Y. Tsuda, and J. Kawaguchi, "Orbit-attitude coupled motion around small bodies: Sun-synchronous orbits with Sun-tracking attitude motion," *Acta Astronautica*, 2017.

[27] Y. Takahashi and D. J. Scheeres, "Small-body postrendezvous characterization via slow hyperbolic flybys," *Journal of Guidance, Control and Dynamics*, Vol. 34, No. 6, 2011, pp. 1815–1827.

[28] R. D. Lorenz and J. Mitton, "Cassini Radar Views the Surface of Titan," Vol. 308, No. May, 2005, pp. 970–975.

[29] M. G. Daly, O. S. Barnouin, C. Dickinson, J. Seabrook, C. L. Johnson, G. Cunningham, T. Haltigin, D. Gaudreau, C. Brunet, I. Aslam, A. Taylor, E. B. Bierhaus, W. Boynton, M. Nolan, and D. S. Lauretta, "The OSIRIS-REx Laser Altimeter (OLA) Investigation and Instrument," *Space Science Reviews*, 2017, 10.1007/s11214-017-0375-3.

[30] Advanced Scientific Concepts, "GoldenEye 3D Flash LIDAR$^{\text{TM}}$ Space Camera,"

[31] V. G. Shevchenko and E. F. Tedesco, "Asteroid albedos deduced from stellar occultations," *Icarus*, Vol. 184, 2006, pp. 211–220, 10.1016/j.icarus.2006.04.006.

[32] R. W. Gaskell, O. S. Barnouin-Jha, D. J. Scheeres, a. S. Konopliv, T. Mukai, S. Abe, J. Saito, M. Ishiguro, T. Kubota, T. Hashimoto, J. Kawaguchi, M. Yoshikawa, K. Shirakawa, T. Kominato, N. Hirata, and H. Demura, "Characterizing and navigating small bodies with imaging data," *Meteoritics and Planetary Science*, Vol. 43, No. 6, 2008, pp. 1049–1061, 10.1111/j.1945-5100.2008.tb00692.x.

[33] F. Castellini, R. P. D. Santayana, K. Vantournhout, and M. Lauer, "Operational Experience and Assessment of the Implementation of the Maplet Technique for Rosetta's Optical Navigation," *AAS/AIAA Astrodynamics Specialist Conference*, 2017, pp. 1–20.

[34] V. Reddy, T. L. Dunn, C. A. Thomas, N. A. Moskovitz, and T. H. Burbine, "Mineralogy and surface composition of asteroids," *Asteroids IV, na*, 2015.

[35] R. P. Binzel, A. Morbidelli, S. Merouane, F. E. DeMeo, M. Birlan, P. Vernazza, C. A. Thomas, A. S. Rivkin, S. J. Bus, and A. T. Tokunaga, "Earth encounters as the origin of fresh surfaces on near-Earth asteroids," *Nature*, Vol. 463, Jan. 2010, pp. 331–334, 10.1038/nature08709.

[36] M. L. Nelson, D. T. Britt, and L. A. Lebofsky, *Review of asteroid compositions.*, pp. 493–522. 1993.

[37] M. J. Gaffey, T. H. Burbine, J. L. Piatek, K. L. Reed, D. A. Chaky, J. F. Bell, and R. H. Brown, "Mineralogical variations within the S-type asteroid class," *ICARUS*, Vol. 106, Dec. 1993, p. 573, 10.1006/icar.1993.1194.

[38] A. Cheng, P. Michel, M. Jutzi, A. Rivkin, A. Stickle, O. Barnouin, C. Ernst, J. Atchison, P. Pravec, D. Richardson, *et al.*, "Asteroid impact & deflection assessment mission: kinetic impactor," *Planetary and space science*, Vol. 121, 2016, pp. 27–35.

[39] A. Stickle, J. Atchison, O. Barnouin, A. Cheng, C. Ernst, Z. Fletcher, D. Richardson, and A. Rivkin, "Modeling momentum transfer from the dart spacecraft impact into the moon of didymos," *Proceedings of the 4th IAA Planetary Defense Conference, Frascati, Italy*, 2015.

[40] J. Sanchez and C. McInnes, "Asteroid resource map for near-Earth space," *Journal of Spacecraft and Rockets*, Vol. 48, No. 1, 2011, p. 153.

[41] B. Rozitis, E. MacLennan, and J. P. Emery, "Cohesive forces prevent the rotational breakup of rubble-pile asteroid (29075) 1950 DA," *Nature*, Vol. 512, No. 7513, 2014.

[42] D. J. Scheeres, C. M. Hartzell, P. Sánchez, and M. Swift, "Scaling forces to asteroid surfaces: The role of cohesion," *Icarus*, Vol. 210, No. 2, 2010, pp. 968–984.

[43] O. Groussin, L. Jorda, A.-T. Auger, E. Kührt, R. Gaskell, C. Capanna, F. Scholten, F. Preusker, P. Lamy, S. Hviid, *et al.*, "Gravitational slopes, geomorphology, and material strengths of the nucleus of comet 67P/Churyumov-Gerasimenko from OSIRIS observations," *Astronomy & Astrophysics*, Vol. 583, 2015, p. A32.

[44] M. H. Poelchau, T. Kenkmann, K. Thoma, T. Hoerth, A. Dufresne, and F. Schäfer, "The MEMIN research unit: Scaling impact cratering experiments in porous sandstones," *Meteoritics & Planetary Science*, Vol. 48, No. 1, 2013, pp. 8–22.

[45] K. Holsapple, "The scaling of impact processes in planetary sciences," *Annual review of earth and planetary sciences*, Vol. 21, No. 1, 1993, pp. 333–373.

[46] J. Biele, S. Ulamec, M. Maibaum, R. Roll, L. Witte, E. Jurado, P. Muñoz, W. Arnold, H.-U. Auster, C. Casas, *et al.*, "The landing (s) of Philae and inferences about comet surface mechanical properties," *Science*, Vol. 349, No. 6247, 2015, p. aaa9816.

[47] K. R. Housen and K. A. Holsapple, "Scale effects in strength-dominated collisions of rocky asteroids," *Icarus*, Vol. 142, No. 1, 1999, pp. 21–33.

MASS BUDGET

Component	Material	Manufacturer/PN For Reference	Coating	Quantity	Mass (g)	Total Comp Mass (g)	% Contingency	Total + Contingency (g)	Subsystem Mass (g)	Reference
Structure									**35166**	
+Z Panel	AL 7075-T7	PRT-MAX-002	8625, Type III, Class1	1	4200	4200	10	4620		50cmx50cmx.6cm
-Z Panel	AL 7075-T7	PRT-MAX-003	8625, Type III, Class1	1	4200	4200	10	4620		50cmx50cmx.6cm
+Y Panel	AL 7075-T7	PRT-MAX-019	8625, Type III, Class1	1	5880	5880	10	6468		50cmx70cmx.6cm
-Y Panel	AL 7075-T7	PRT-MAX-001	8625, Type III, Class1	1	5880	5880	10	6468		50cmx70cmx.6cm
+X Panel	AL 7075-T7	PRT-MAX-004	8625, Type III, Class1	1	5880	5880	10	6468		50cmx70cmx.6cm
-X Panel	AL 7075-T7	PRT-MAX-005	8625, Type III, Class1	1	5880	5880	10	6468		50cmx70cmx.6cm
Battery Housing	AL 6061-T651			1	45	45	20	54		
Antennas									**4025**	
X-Band Patch Antennas				6	50	300	15	345		
Feed Horn				1	200	200	15	230		
Reflectarray Panel	RT Duroid 5880LZ			1	3000	3000	15	3450		
Bus Components									**68514**	
Solar Array 450W	PCB/Solar Cells			1	6000	6000	10	6600		
BCT XB MicroSat System	PCB	Blue Canyon Technology		1	7500	7500	5	7875		Includes ADCS sensor suite with Star Trackers
X-Band Radio Board				1	400	400	15	460		
8cm Xenon Ion Propulsion System (XIPS)		BHT-600		4	2000	8000	5	8400		
XiPS thruster PPU		600W BHT-600		2	7000	14000	5	14700		
Tank Propulasion Wet Mass				1	19000	19000	10	20900		
Pulsed plasma thruster				6	200	1200	10	1320		
Reaction Wheel System		BCT RW1		3	1600	4800	5	5040		
Tri-Driectional Sun Sensors				6	10	60	15	69		
2 Cell Battery Packs				30	100	3000	5	3150		
Payloads									**27203**	
Argus Spectrometer				1	230	230	10	253		
AMICA Camera				1	5740	5740	10	6314		
Altimeter				1	3560	3560	10	3916		
Explosive System				1	2200	2200	35	2970		
Narrow Angle Camera				1	11000	11000	25	13750		
Fasteners				1	1000	1000	15	1150	**1150**	
Harness				1	2000	2000	15	2300	**2300**	Includes SMA Cables
Staking/Coating				1	1000	1000	15	1150	**1150**	
						Total			**139508**	
						Total Mass Allowed			**140000**	
						Mass Remaining			492	

LINK BUDGET

Uplink Budget
ATLAS to Spacecraft @ 5221 MHz (C-band)

Parameter	Units	Values			
Uplink Frequency	MHz	5221	5221	5221	5221
Slant Range	km	4 000 000	6 000 000	27 000 000	34 732 248
Boltzmann's constant	J/°K	1,381E-23	1,381E-23	1,381E-23	1,381E-23
Transmit Station Parameters					
Transmitter power	W	3000	3000	3000	3000
Feeder Losses	dB	4,1	4,1	4,1	4,1
Antenna Gain	dBi	50,3	50,3	50,3	50,3
Transmit EIRP	dBm	110,97	110,47	110,47	110,47
Tx Station Polarization Loss	dB	0,5	0,5	0,5	0,5
Tx Station Pointing Loss	dB	0,5	0,5	0,5	0,5
Propagation Parameters					
Free Space Loss	dB	238,8	242,4	255,4	257,6
Clear Sky Atmospheric Loss	dB	0,5	0,5	0,5	0,5
Receive Station Parameters					
Antenna Gain	dBi	6,0	6,0	6,0	6,0
Antenna Efficiency	%	75	75	75	75
Receiver System Noise Temperature (Te)	°K	1802	1802	1802	1802
Receiver Noise Figure	dB	8,5	8,5	8,5	8,5
Receiver G/T	dB/°K	1,3	1,3	1,3	1,3
Receiver Noise Power Density (No)	dBm/Hz	-126,4	-126,4	-126,4	-126,4
Carrier parameters					
Required Eb/No for 10-5 BER using FSK	dB	9,8	9,8	9,8	9,8
Modulation	-	FSK	FSK	FSK	FSK
Coding Gain	dB	1,5	1,5	1,5	1,5
Required Eb/No for 10-5 BER using FSK with Coding Gain	dB	8,3	8,3	8,3	8,3
Useful bit rate	**bits/s**	**46**	**18**	**1**	**0,55**
Symbol rate (R)	sym/s	46	18	1	1
Symbol period (Ts)	msec	21,74	55,56	1000,00	1818,18
Modem filter Roll-off	%	20	20	20	20
Carrier bandwidth	Hz	55	22	1	1
Results					
Received Signal Power (S)	**dBm**	**-95,5**	**-99,5**	**-112,6**	**-114,7**
Received Noise Power (N)	**dBm**	**-56,1**	**-56,1**	**-56,1**	**-56,1**
Received SNR	**dB**	**-39,4**	**-43,4**	**-56,5**	**-58,7**
Received Eb	**dBJ**	**-112,1**	**-112,0**	**-112,6**	**-112,1**
Received No	**dBm/Hz**	**-126,4**	**-126,4**	**-126,4**	**-126,4**
Resulting Eb/No	**dB**	**14,3**	**14,3**	**13,8**	**14,2**
Link Margin	**dB**	**5,98**	**6,04**	**5,52**	**5,93**

Downlink Budget @ 4 million km
Spacecraft to ATLAS @ 8400 MHz (X-band)

Parameter	Units	Values	
Tx Antenna	-	Reflect Array	FeedHorn
Downlink Frequency	MHz	8447,6	8447,6
Slant Range	km	4 000 000	4 000 000
Transmit Station Parameters			
Transmitter power	dBm	48,5	48,5
Transmitter power	W	70,0	70,0
Feed Loss	dB	1,8	1,8
Antenna Gain	dBi	23,0	12,8
Transmit EIRP	dBm	69,65	59,45
Tx Station Polarization Loss	dB	0,5	0,5
Tx Station Pointing Loss	dB	0,5	0,5
Propagation Parameters			
Free Space Loss	dB	243,0	243,0
Clear Sky Atmospheric Loss	dB	0,5	0,5
Receive Station Parameters			
Rx Station Pointing Loss	dB	0,5	0,5
Rx Station Polarization Loss	dB	0,5	0,5
Antenna Gain	dBi	54,3	54,3
Receiver G/T	dB/°K	29,0	29,0
Receiver Noise Temperature (Te)	°K	338,8	338,8
Receiver Noise Figure	dB	3,3	3,3
Receiver Noise Power Density (No)	dBm/Hz	-173,3	-173,3
Carrier parameters			
Required Eb/No for 10-5 BER using QPSK	dB	9,6	9,6
Coding Gain	dB	1,5	1,5
Required Eb/No for 10-5 BER using QPSK with Coding Gain	dB	8,1	8,1
Useful bit rate	**bits/s**	**11592**	**1107**
Symbol rate (R)	sym/s	5796	554
Symbol Period (Ts)	msec	0,17	1,81
Modem filter Roll-off	%	20	20
Carrier bandwidth	Hz	6955	664
Results			
Received Signal Power (S)	**dBm**	**-121,6**	**-131,8**
Received Noise Power (N)	**dBm**	**-113,3**	**-113,3**
Received SNR	**dB**	**-8,3**	**-18,5**
Received Eb	**dBmJ**	**-159,2**	**-159,2**
Received No	**dBm/Hz**	**-173,3**	**-173,3**
Resulting Eb/No	**dB**	**14,1**	**14,1**
Link Margin	**dB**	**6,00**	**6,00**

Downlink Budget @ 6 million km
Spacecraft to ATLAS @ 8400 MHz (X-band)

Parameter	Units	Values	
Tx Antenna	-	Reflect Array	FeedHorn
Downlink Frequency	MHz	8447,6	8447,6
Slant Range	km	6 000 000	6 000 000
Transmit Station Parameters			
Transmitter power	dBm	48,5	48,5
Transmitter power	W	70,0	70,0
Feed Loss	dB	1,8	1,8
Antenna Gain	dBi	23,0	12,8
Transmit EIRP	dBm	69,65	59,45
Tx Station Polarization Loss	dB	0,5	0,5
Tx Station Pointing Loss	dB	0,5	0,5
Propagation Parameters			
Free Space Loss	dB	246,5	246,5
Clear Sky Atmospheric Loss	dB	0,5	0,5
Receive Station Parameters			
Rx Station Pointing Loss	dB	0,5	0,5
Rx Station Polarization Loss	dB	0,5	0,5
Antenna Gain	dBi	54,3	54,3
Receiver G/T	dB/°K	29,0	29,0
Receiver Noise Temperature (Te)	°K	338,8	338,8
Receiver Noise Figure	dB	3,3	3,3
Receiver Noise Power Density (No)	dBm/Hz	-173,3	-173,3
Carrier parameters			
Required Eb/No for 10-5 BER using QPSK	dB	9,6	9,6
Coding Gain	dB	1,5	1,5
Required Eb/No for 10-5 BER using QPSK with Coding Gain	dB	8,1	8,1
Useful bit rate	**bits/s**	**5152**	**492**
Symbol rate (R)	sym/s	2576	246
Symbol Period (Ts)	msec	0,39	4,07
Modem filter Roll-off	%	20	20
Carrier bandwidth	Hz	3091	295
Results			
Received Signal Power (S)	**dBm**	**-125,1**	**-135,3**
Received Noise Power (N)	**dBm**	**-113,3**	**-113,3**
Received SNR	**dB**	**-11,8**	**-22,0**
Received Eb	**dBmJ**	**-159,2**	**-159,2**
Received No	**dBm/Hz**	**-173,3**	**-173,3**
Resulting Eb/No	**dB**	**14,1**	**14,1**
Link Margin	**dB**	**6,00**	**6,00**

Downlink Budget @ 27 million km
Spacecraft to ATLAS @ 8400 MHz (X-band)

Parameter	Units	Values	
Tx Antenna	-	Reflect Array	FeedHorn
Downlink Frequency	MHz	8447,6	8447,6
Slant Range	km	27 000 000	27 000 000
Transmit Station Parameters			
Transmitter power	dBm	48,5	48,5
Transmitter power	W	70,0	70,0
Feed Loss	dB	1,8	1,8
Antenna Gain	dBi	23,0	12,8
Transmit EIRP	dBm	69,65	59,45
Tx Station Polarization Loss	dB	0,5	0,5
Tx Station Pointing Loss	dB	0,5	0,5
Propagation Parameters			
Free Space Loss	dB	259,6	259,6
Clear Sky Atmospheric Loss	dB	0,5	0,5
Receive Station Parameters			
Rx Station Pointing Loss	dB	0,5	0,5
Rx Station Polarization Loss	dB	0,5	0,5
Antenna Gain	dBi	54,3	54,3
Receiver G/T	dB/°K	29,0	29,0
Receiver Noise Temperature (Te)	°K	338,8	338,8
Receiver Noise Figure	dB	3,3	3,3
Receiver Noise Power Density (No)	dBm/Hz	-173,3	-173,3
Carrier parameters			
Required Eb/No for 10-5 BER using QPSK	dB	9,6	9,6
Coding Gain	dB	1,5	1,5
Required Eb/No for 10-5 BER using QPSK with Coding Gain	dB	8,1	8,1
Useful bit rate	**bits/s**	**254,5**	**24,3**
Symbol rate (R)	sym/s	127	12
Symbol Period (Ts)	msec	7,86	82,30
Modem filter Roll-off	%	20	20
Carrier bandwidth	Hz	153	15
Results			
Received Signal Power (S)	**dBm**	**-138,2**	**-148,4**
Received Noise Power (N)	**dBm**	**-113,3**	**-113,3**
Received SNR	**dB**	**-24,9**	**-35,1**
Received Eb	**dBmJ**	**-159,2**	**-159,2**
Received No	**dBm/Hz**	**-173,3**	**-173,3**
Resulting Eb/No	**dB**	**14,1**	**14,1**
Link Margin	**dB**	**6,00**	**6,00**

Downlink Budget @ 35 million km
Spacecraft @ HO3 arrival to ATLAS @ 8400 MHz (X-band)

Parameter	Units	Values	
Tx Antenna	-	Reflect Array	FeedHorn
Downlink Frequency	MHz	8447,6	8447,6
Slant Range	km	34732248	34732248
Transmit Station Parameters			
Transmitter power	dBm	48,5	48,5
Transmitter power	W	70,0	70,0
Feed Loss	dB	1,8	1,8
Antenna Gain	dBi	23,0	12,8
Transmit EIRP	dBm	69,65	59,45
Tx Station Polarization Loss	dB	0,5	0,5
Tx Station Pointing Loss	dB	0,5	0,5
Propagation Parameters			
Free Space Loss	dB	261,8	261,8
Clear Sky Atmospheric Loss	dB	0,5	0,5
Receive Station Parameters			
Rx Station Pointing Loss	dB	0,5	0,5
Rx Station Polarization Loss	dB	0,5	0,5
Antenna Gain	dBi	54,3	54,3
Receiver G/T	dB/°K	29,0	29,0
Receiver Noise Temperature (Te)	°K	338,8	338,8
Receiver Noise Figure	dB	3,3	3,3
Receiver Noise Power Density (No)	dBm/Hz	-173,3	-173,3
Carrier parameters			
Required Eb/No for 10-5 BER using QPSK	dB	9,6	9,6
Coding Gain	dB	1,5	1,5
Required Eb/No for 10-5 BER using QPSK with Coding Gain	dB	8,1	8,1
Useful bit rate	**bits/s**	**153,8**	**14,7**
Symbol rate (R)	sym/s	77	7
Symbol Period (Ts)	msec	13,00	136,05
Modem filter Roll-off	%	20	20
Carrier bandwidth	Hz	92	9
Results			
Received Signal Power (S)	**dBm**	**-140,3**	**-150,5**
Received Noise Power (N)	**dBm**	**-113,3**	**-113,3**
Received SNR	**dB**	**-27,0**	**-37,2**
Received Eb	**dBmJ**	**-159,2**	**-159,2**
Received No	**dBm/Hz**	**-173,3**	**-173,3**
Resulting Eb/No	**dB**	**14,1**	**14,1**
Link Margin	**dB**	**6,00**	**6,00**

POWER BUDGET

Spacecraft Subsystem, Unit, Quantity and Power Consumption												Power Consumption by Spacecraft Mode									
Subsystem	Component/ Use Case	Voltage (V)	Current (A)	Peak Power(W)	Contingency (%)	Peak Power (W) + Contingency	Qty	Comment	Total Power Per Hour (W)	Pheonix		Sleep		Cruise		Safe		Nominal		Payload Demo	
										Duty Cycle	Mode Power	Duty Cycle	Mode Power	Duty Cycle	Mode Power	Duty Cycle	Mode Power	Duty Cycle	Mode Power	Duty Cycle	Mode Power
Core Avionics																					
CDH	Nominal	3.50	0.03	0.11	5.00	0.11	1		0.11	100.00%	0.11	100.00%	0.11	100.00%	0.11	100.00%	0.11	100.00%	0.11	100.00%	0.11
Payload CDH	Nominal	3.50	0.07	0.25	15.00	0.28	1		0.28	0.00%	0.00	0.00%	0.00	100.00%	0.28	100.00%	0.28	100.00%	0.28	100.00%	0.28
LOS	Radio TX	8.40	1.25	10.50	5.00	11.03	1		11.025	10.00%	1.10	0.00%	0.00	10.00%	1.10	10.00%	1.10	10.00%	1.10	10.00%	1.10
	Radio RX	3.50	0.10	0.35	5.00	0.37	1		0.3675	100.00%	0.37	0.00%	0.00	100.00%	0.37	100.00%	0.37	100.00%	0.37	100.00%	0.37
X-Band	HRCCS TX	7V		350.00	25.00	437.50	1		437.5	0.00%	0.00	0.00%	0.00	0.00%	0.00	0.00%	0.00	50.00%	218.75	0.00%	0.00
	RF Switch			2.76	15.00	3.17	1		3.174	0.00%	0.00	0.00%	0.00	0.00%	0.00	0.00%	0.00	2.00%	0.06	0.00%	0.00
ADCS	Nominal	5.00	0.50	2.50	5.00	2.63	1		2.625	0.00%	0.00	0.00%	0.00	100.00%	2.63	100.00%	2.63	100.00%	2.63	100.00%	2.63
	Reaction Wheel System (3 Wheels)	12.00		7.00	15.00	8.05	3		24.15	0.00%	0.00	0.00%	0.00	50.00%	12.08	50.00%	12.08	50.00%	12.08	50.00%	12.08
	Torque Rods			0.50	15.00	0.58	3		1.725	0.00%	0.00	0.00%	0.00	5.00%	0.09	5.00%	0.09	5.00%	0.09	5.00%	0.09
EPS	Power System	8.40	0.03	0.25	5.00	0.26	1		0.2646	100.00%	0.26	100.00%	0.26	100.00%	0.26	100.00%	0.26	100.00%	0.26	100.00%	0.26
	Propulsion			300.00	10.00	330.00	1		330	0.00%	0.00	0.00%	0.00	100.00%	330.00	0.00%	0.00	5.00%	16.50	0.00%	0.00
	Heaters	8.40	0.53	4.41	5.00	4.63	20		92.61	0.00%	0.00	0.00%	0.00	10.00%	9.26	10.00%	9.26	10.00%	9.26	10.00%	9.26
Payloads																					
Argus	Nominal	4.20	0.36	1.51	15.00	1.74	1		1.74	0.00%	0.00	0.00%	0.00	0.00%	0.00	0.00%	0.00	0.00%	0.00	15.00%	0.26
AMICA	Nominal	8.40		16.30	15.00	18.75	1		18.75	0.00%	0.00	0.00%	0.00	0.00%	0.00	0.00%	0.00	0.00%	0.00	15.00%	2.81
NAC	Nominal	12.00		15.00	15.00	17.25	1		17.25	0.00%	0.00	0.00%	0.00	0.00%	0.00	0.00%	0.00	0.00%	0.00	15.00%	2.59
Altimeter	Nominal	8.40		22.00	15.00	25.30	1		25.3	0.00%	0.00	0.00%	0.00	0.00%	0.00	0.00%	0.00	0.00%	0.00	15.00%	3.80
Explosive System	Nominal	5.00		3.00	15.00	3.45	1		3.45	0.00%	0.00	0.00%	0.00	0.00%	0.00	0.00%	0.00	0.00%	0.00	1.00%	0.03
Total Mode Power Per Orbit (W)										1.84		0.37		356.17		26.17		261.49		35.66	

Power Regulation	
MPPT Efficiency	0.85
Average Regulator Efficiency	0.85
Total Power System Efficiency	0.7225

Storage						
Cell Voltage (V)	Cell Capacity (Ah)	Series Cells/String	# of Strings	Pack Voltage (V)	Pack Capacity (Ah)	Pack Power (Wh)
4.2	3.35	2	30	8.4	100.5	844.2

Generated Power via Power Generated Area

Item	Value	Unit	Equation	Note
Solar Cell Efficiency	0.32	%		
Inherent Degeneration (EOL)	0.8	%		With Coverglass. 5 Year
Solar Constant	1367	W		
Average Sun Angle	90	Deg		Sun Point Mode
Generated Power per Square Meter	349.9519	W	P = SCeff *Id *SC* sin(a)	
Area per Cell	0.002662	m^2		
Number of Cells	425	#		
Total Solar Cell Area	1.13135			
Generated Power	395.9181	W	Ptotal = P*TotalA	
Sunlight per Orbit	1	hour(s)		
Available Power Per Orbit	395.9181	W		